Protonation States of Novel Therapeutics for the Resurrection of Organophosphorus-Aged Acetylcholinesterase

Thesis

Presented in Partial Fulfillment of the Requirements for the Degree Master of Science in the Graduate School of The Ohio State University

By:

Ryan G. Hopf

Graduate Program in Chemistry

The Ohio State University

2020

Thesis Committee:

Dr. Christopher M. Hadad, Advisor

Dr. Jon R. Parquette, Member

Abstract

Acetylcholinesterase (AChE) is an enzyme which catalyzes the degradation of acetylcholine to acetic acid and choline within neuromuscular junctions. Upon inhibition of AChE by some toxicant, acetylcholine begins to build up at the neuromuscular junctions and results in a cholinergic crisis, resulting in a variety of symptoms which can be summarized by the SLUDGE acronym: salivation, lacrimation, urination, defecation, gastrointestinal distress, and emesis. Left untreated and if toxic exposure is sufficient, a cholinergic crisis will result in death.

While a non-lethal cholinergic crisis can result from a variety of triggers, organophosphorus (OP) compounds pose a global threat to human populations. Responsible for approximately 200,000 deaths annually, OP compounds inhibit AChE via phosphylation of a serine residue situated within the active site of AChE. Current medical treatment for inhibited AChE involves the use of nucleophilic oximes, which displace the phosphorus species. Individuals exposed to OPs are also given a variety of other medicines to treat the SLUDGE symptoms described above.

Although the use of a nucleophilic oxime can displace the phosphorus moiety, OP-inhibited AChE can also undergo a process known as aging. Aging occurs when the phosphorus moiety undergoes spontaneous *O*-dealkylation. Once AChE has aged, the phosphorus center is less electrophilic which limits the use of a nucleophilic treatment such as pyridinium oximes. Currently, there is no approved therapeutic which can restore aged AChE to the native state.

Our group has recently shown that quinone methide precursors (QMPs) can both resurrect OP-aged AChE and reactive OP-inhibited AChE back to the native state of the enzyme. However, the ability of a QMP to resurrect OP-aged AChE and reactive OP-inhibited AChE has been shown to be dependent on the amine leaving group of the QMP. More recently, computational efforts by Joseph Fernandez, a graduate student on our research team, have indicated that the protonation state of our QMPs may also impact the ability of a QMP to resurrect OP-aged AChE and reactive OP-inhibited AChE. Ola Nosseir, another member of our research group, has used EPIK to generate preliminary protonation state assignments for our QMPs at physiological pH. The work in this thesis describes the use of an FT-IR and ^{1}H NMR spectroscopic methods in order to provide experimental data so as to confirm the assignments made by the EPIK program.

Initial protonation state assignments were simply based on simplistic pK_a assignments generated from ^{1}H NMR data. These pK_a assignments were generated by plotting the chemical shift of various hydrogens of our QMPs versus the pH of an aqueous solution. As the pH of a solution is increased, the deprotonation of a titratable proton causes an upfield shift for other protons in the molecule. When these chemical shifts are graphed, these deprotonation events are indicated by a sigmoidal curve. These sigmoidal curves are known to represent the pK_a values for the various titratable protons found in the molecule.

However, while appropriate for initial protonation state assignments, this method is quite crude as the assignments are only based on chemical intuition and knowledge of various pK_a values. Thus, we sought additional experimental data, which could be corroborated computationally, to confirm our protonation state assignments.

First, we report that the $^4J_{H\text{-}H}$ meta coupling constants on the aromatic ring can also be used to assign the protonation state of a molecule. Like the chemical shift data described above, the $^4J_{H\text{-}H}$ meta coupling constants can be plotted versus the pH of an aqueous solution to generate sigmoidal curves. These sigmoidal curves were found to occur at the same pH as the sigmoidal curves described earlier and were consequently associated with deprotonation events of titratable protons.

We initially chose to probe the $^4J_{H\text{-}H}$ meta coupling constants found in two of our core frameworks. Calculated $^4J_{H\text{-}H}$ meta coupling constants for all protonation states for these frameworks were generated at the B3LYP/aug-cc-pvtz level of theory. Notably, at both low and high pH, the calculated $^4J_{H\text{-}H}$ meta coupling constants for the fully protonated and deprotonated forms our frameworks were in agreeance with the experimental $^4J_{H\text{-}H}$ meta coupling constants obtained at an appropriate pH.

The initial success in using the $^4J_{H\text{-}H}$ meta coupling constants to assign protonation states for our core frameworks, prompted us to investigate the couplings of a model QMP. Thus, the coupling constants for the various protonation states of a model QMP were calculated and compared to experimental data. Like the core frameworks, at both low and high pH, the calculated $^4J_{H\text{-}H}$ meta coupling constants for

the fully protonated and deprotonated forms of this model QMP agreed with the experimental coupling constants. We then hypothesized that the $^{4}J_{H\text{-}H}$ meta coupling constants of this model QMP near physiological pH might agree well with the calculated coupling constants of one of the protonation states. The comparison of the $^{4}J_{H\text{-}H}$ meta coupling constant of this model QMP near physiological pH was found to agree well with the calculated $^{4}J_{H\text{-}H}$ meta coupling constants obtained from the QMP in a zwitter-ionic protonation state.

While ^{1}H NMR provided preliminary protonation state assignments, we also report that experimental IR spectroscopy can be used to corroborate our protonation state assignment. To make this assignment, Boltzmann distributions for each possible protonation state of the same model QMP from above were computed at the B3LYP/6-311+G(d,p) level of theory. These different Boltzmann distributions were then compared to an experimental IR spectrum obtained near physiological pH. After considering the effects of intramolecular hydrogen bonding, the Boltzmann distribution of two distinct zwitter-ionic forms was found to represent the experimental IR (taken near physiological pH) of our model QMP.

Dedication

This document is dedicated to my grandfather Kenny Hopf. As a young child working on a family farm, Kenny was responsible for taking care of the chickens and as such used harmful insecticides long before the dangers of these compounds were known. One such compound that was often used on the farm was methyl parathion, an organophosphorus insecticide, which is now known to have profound links to Parkinson's Disease. Kenny passed away in 2014 from complications associated with Parkinson's Disease.

Acknowledgements

To my friends and family who have helped and supported me on my journey thus far, all I can say is thank you.

To my advisor Dr. Christopher Hadad – while I wish that I could type out all of the ways that I am thankful for the experiences that you have given me, I believe that the list would be to long for this acknowledgements section. I've truly enjoyed my time at The Ohio State University, and I attribute this to the way that you inspire, work with, teach, and treat your graduate students. I am extremely grateful that I was able to be a member of the Hadad Lab for my brief time at The Ohio State University, thank you.

To Dr. Christopher Callam and Dr. Craig McElroy – thank you for your invaluable suggestions and comments. Additionally, I would like to add that I think you are both brilliant educators and truly better not only The Ohio State University, but every student that is fortunate enough to learn from you.

To Rémy Lalisse and Joe Fernandez, thank you for the help and guidance that you provided in the regards to computational chemistry. Additionally, I thoroughly enjoyed our many conversations in the fourth-floor office which were often times unrelated to chemistry.

To Rémy Lalisse, Dr. Sarah Border, and Taylor Hamby – thank you for your friendship. I greatly enjoyed our time not only rock climbing, but also at Buffalo Wild Wings. I look forward to visiting Columbus again and rock climbing with you all at some point in the future.

To everyone in the Hadad, Callam, and Dogan Ekici groups – especially Ben Clark, and those mentioned above - thank you for making the work environment so much fun every day. One would only have to sit in on one of our group meetings for a few minutes to realized how phenomenal everyone is. Ben, I apologize for leaving our softball team without its star player.

To my parents, Greg and Karla Hopf, thank you for your love and support for not just these past two years, but my entire life. Knowing that you have both been in my corner, and by my side, from day one has been a tremendous comfort, even if I don't say it as often as I should. I truly appreciate everything you have both done to help Brett and I in life. All I can really say is, thank you, and I love you both.

To my best friend and partner Angela DaCosta, I cannot truly express how thankful I am for your love and support during this journey. I'm not sure that I could have done it without you. I love you.

Vita

2016……..B.S. Chemistry (ACS Certified) University of Southern Indiana

2017 – 2019……Graduate Teaching Assistant, Department of Chemistry and Biochemistry, The Ohio State University

Publications

1. Pavlović, R. Z.; Zhiquan, L.; Güney, M.; Lalisse, R. F.; Hopf, R. G.; Gallucci, J.; Moore, C.; Xie, H.; Hadad, C. M.; Badjić, J. D. "Multivalent C−H···Cl/Br−C Interactions Directing the Resolution of Dynamic and Twisted Capsules" *Chem. Eur. J.* **2019**, *25*, 13124 – 13130.
   DOI: 10.1002/chem.201903006

Fields of Study

Major Field: Chemistry

Table of Contents

List of Tables

List of Figures

Chapter 1: Introduction

Acetylcholinesterase (AChE) is a biologically important enzyme. The core function of AChE is to hydrolyze the neurotransmitter acetylcholine (ACh) at nerve synapses. This hydrolysis terminates the signal that ACh has transmitted from a nerve to a post-synaptic membrane. Upon inhibition of AChE by some toxicant, ACh is no longer hydrolyzed and a variety of muscarinic symptoms begin to present. Commonly, these symptoms are referred as SLUDGE, where SLUDGE is an acronym for: salivation, lacrimation, urination, defecation, GI symptoms, and emesis. Left untreated, significant AChE inhibition will result in death.

Unfortunately, several effective AChE inhibitors are known. The most common are the organophosphate pesticides known as paraoxon methyl (PM), paraoxon ethyl (PE), and diisopropyl fluorophosphate (DFP), which are shown below (**Figure 1.1**). The organophosphates shown in Figure 1.1, as well as several closely related compounds, are commonly used in third world countries as pesticides. While the compounds function as pesticides, they also have a more nefarious use and account for approximately 250,000 suicides annually. Sadly, the 250,000 annual death toll is likely underreported, and this number is likely closer to 370,000.[1] Thus, out of an estimated annual 873,000 suicides around the globe, OP pesticides can account for approximately 30% of these.[1]

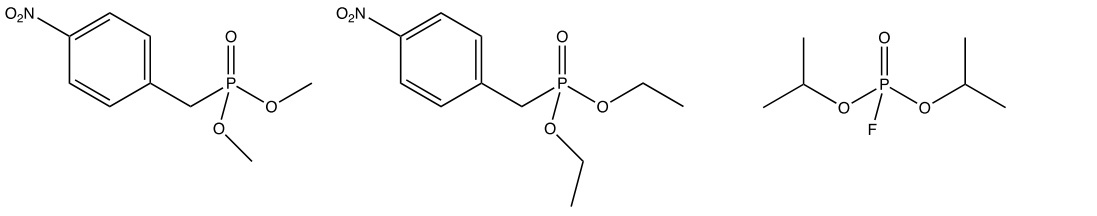

Figure 1.1 Structures of PM, PE, and DFP

While OP pesticides result in a staggering number of annual deaths, another class of OP compounds, methylphosphonates, cause far fewer annual deaths, but pose significant threats to civilian and military populations. Known as OP chemical nerve agents, these species are significantly more toxic than the OP pesticides and can lead to the shutdown of the central nervous system (CNS), causing death, within 20 minutes.

The first reported OP nerve agent synthesis can be traced back to Gerhard Schrader while he was employed by the German conglomerate IG Farben in 1936 and he was attempting to develop phosphorus- and cyanide-based pesticides. Schrader's initial preparation was initially known as preparation 9/91.[2] Within one year, the IG conglomerate had recognized the lethality of preparation 9/91 and alerted the German state who quickly recognized the potential military uses of the compound.[2] Preparation 9/91 was eventually renamed tabun, based off of the German word for "taboo".

Schrader continued to develop structural variants of tabun for IG Farben. In 1939, Schrader had another breakthrough and synthesized sarin. After extensive testing, sarin was found to be more volatile than tabun, while being twice as lethal. Other German scientists also had success in developing OP nerve agents. In 1943, Richard Kuhn, a Nobel Laureate, synthesized soman, which was found to be more toxic than sarin.[2]

The compounds that both Schrader and Kuhn synthesized have since been classified as G-series nerve agents, where the "G" represents "German." Unfortunately, after World War II, other countries discovered new nerve agents and these agents are classified as "V" agents. Unlike the G-series agents, the "V" simply stands for "venomous" due to the increased toxicity

of these newly found species. Of these new V agents, VX, created by researchers at the Porton Down facility in the United Kingdom, has been shown to be one of the most toxic. VX is nearly three times more toxic than sarin when inhaled, and nearly one thousand times more toxic than sarin when absorbed through the skin. VX also has a low volatility and can be readily deployed as an aerosol. Frighteningly, VX also has no odor which makes the detection of this species notably more difficult. Unfortunately, during the Cold War, the United States began to stockpile VX, while Russia stockpiled an isomer known as VR[2,3] and continued to nefariously develop new nerve agents. Notably, a new class of nerve agents known as Novichoks, meaning "newcomer" in Russian, have been developed. The Novichok agents are purported to be five to eight times more lethal than VX.[4] The aforementioned OP nerve agent structures, excluding the Novichoks, are shown below (**Figure 1.2**).

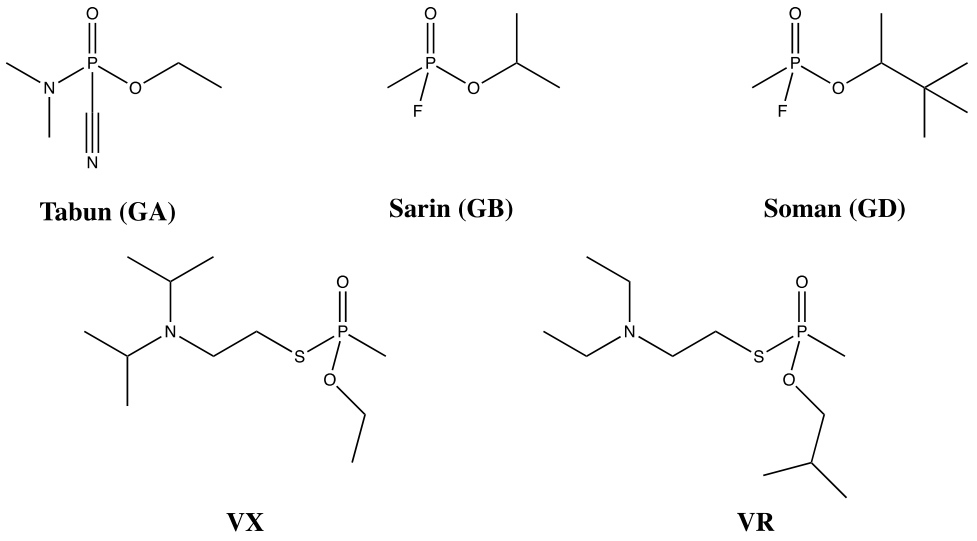

Figure 1.2 Structures of common nerve agents

Although the vast majority of annual OP related deaths are attributed to pesticides, nerve agents have been used by governments, and terrorist organizations, to cause casualties

to civilians and military personnel alike. Perhaps the most notorious use by a government occurred during the Iran-Iraq war when the Iraqi government deployed over 600 tons of sarin against Iranian militants and civilians, resulting in approximately 5,000 deaths and nearly 100,000 injuries.[6,7] While thousands died as a direct result of nerve agent exposure, the death toll has continued to rise as the long-term effects of OP exposure continue to cause fatalities.

Iraq is not the only government to use nerve agents on the battlefield. In 2013, the Syrian government used sarin in a chemical attack against occupants of the city of Ghoutta, killing more than 1,000 people and incapacitating approximately 3,600.[7] More recently, in 2017, the Syrian government again used OP agents against militants and civilians alike located in a number of suburbs surrounding the city of Damascus.[8]

Unfortunately, not only have OPs been used against civilians and military personal, they have also been used by foreign governments for assassinations. Notably, Kim Jong-nam was assassinated when two women smeared binary VX precursors on his face at the Kuala Lumpur airport in Malaysia. The women were recruited by four men identified as North Koreans to play "pranks" on unsuspecting passengers at airports. Purportedly, the two women had "pranked" several other individuals by dumping liquid on them or by wrapping their arms around unsuspecting passengers only weeks before the assassination. The murder charges against the two women were eventually dropped and both women are now out of prison.[10,11]

In 2018, Sergei Skripal, a former Russian spy, who began working for four intelligence agencies of NATO countries, came under attack along with his daughter Yulia. While sitting on a park bench in Salisbury, the pair were found after exposure to a Novichok agent; fortunately,

both of the Skripals survived the attack.[12] Unfortunately, another couple from a city neighboring Salisbury were exposed to the Novichok agent several months later. The couple, Charlie Rowley and Dawn Sturgess, had found a perfume bottle in the same park where the Skripals were found.[13] Sturgess eventually sprayed herself with the compound and was quickly taken to the hospital and admitted. Her partner, Rowley, who only picked up the bottle, also fell ill and was taken to the hospital. Although Rowley has since recovered, Sturgess passed away after exposure to the Novichok agent. After extensive chemical testing, the Organization for the Prohibition of Chemical Weapons (OPCW) confirmed that the poison used against Rowley and Sturgess was the same compound with which the Skripals were exposed.[14]

Dawn Sturgess, along with several thousand other unnamed women, men, and children, have died after being exposed to OP nerve agents. The toxicity of OP compounds lies in their ability to inhibit the enzyme AChE. Upon AChE inhibition, the neurotransmitter ACh is no longer hydrolyzed at neurosynaptic junctions. ACh begins to rapidly build up at these junctions, resulting in overstimulation of the synapses, which rapidly leads to a cholinergic crisis, and if left untreated, death.

More specifically, the OP agent inhibits the serine residue found in the active site of AChE, where the active site is at the bottom of a 20 Å gorge. This serine residue (S203) as well as a histidine (H447) and glutamate (E334) make up the catalytic triad and are responsible for the hydrolysis of ACh in native AChE. In the native (uninhibited) form of the AChE enzyme, S203 performs a nucleophilic attack on the carbonyl carbon of acetylcholine which results in a tetrahedral intermediate. With the aid of a proton transfer from H447, this tetrahedral

intermediate then collapses to reform the carbonyl group, expelling choline as a leaving group. H447 can then activate a water molecule for attack on the carbonyl carbon, thereby forming another tetrahedral intermediate. Upon collapse, the serine oxygen is expelled as a leaving group while also producing acetic acid (**Figure 1.3**). While not directly involved, E334 is thought to stabilize the histidinium species.[15,16]

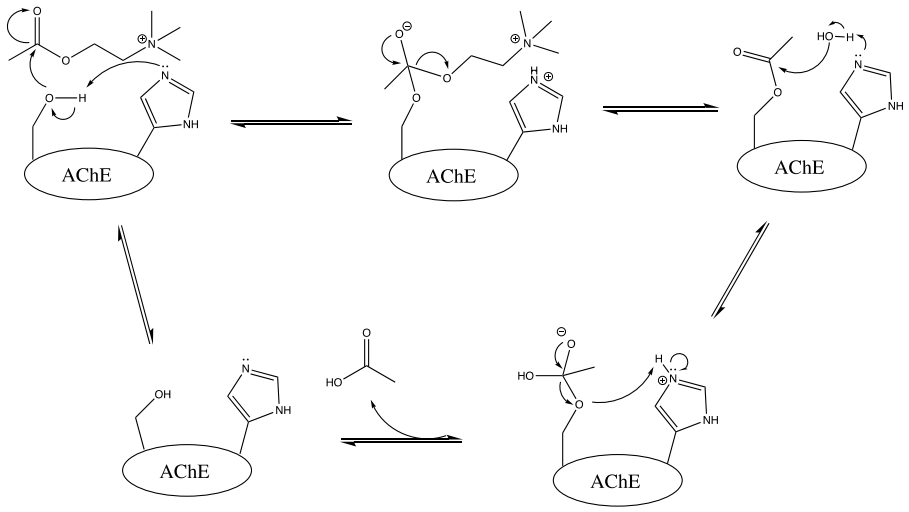

Figure 1.3 Hydrolysis of ACh by native AChE

Currently, individuals exposed to an OP are prescribed a variety of different medications. Some of these medications, such as atropine and diazepam (**Figure 1.4**), are prescribed to treat the symptoms of OP exposure. Atropine, an antimuscarinic drug, prevents the overstimulation of muscarinic nerve receptors by binding to the nicotinic receptors, while diazepam functions to prevent muscle spasms. One should note that neither diazepam nor atropine directly treat the underlying cause of the symptoms, the OP.

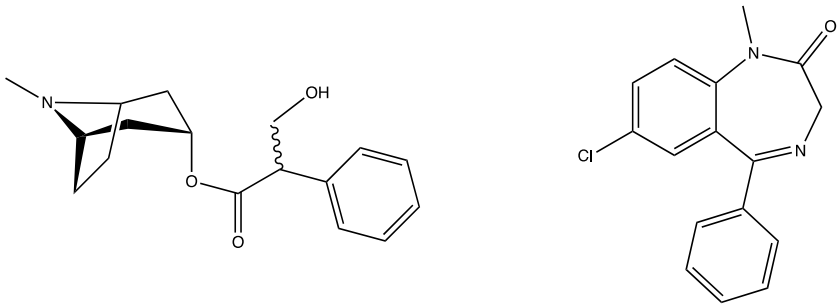

Atropine **Diazepam**

Figure 1.4 Atropine and Diazepam

To treat the underlying cause of the symptoms, patients are also given an oxime. The deprotonated form of the oxime, referred to as an oximate, can perform a nucleophilic addition to the OP-serine adduct. Upon collapse of the pentavalent intermediate, and expulsion of the OP-oxime adduct, the native function of AChE is restored (**Figure 1.5**). Going forward, this process of restoring the native function of AChE to an OP-inhibited form of AChE will be referred to as *reactivation* and the OP-serine adduct will be referred to as the *inhibited* form of the enzyme.[20]

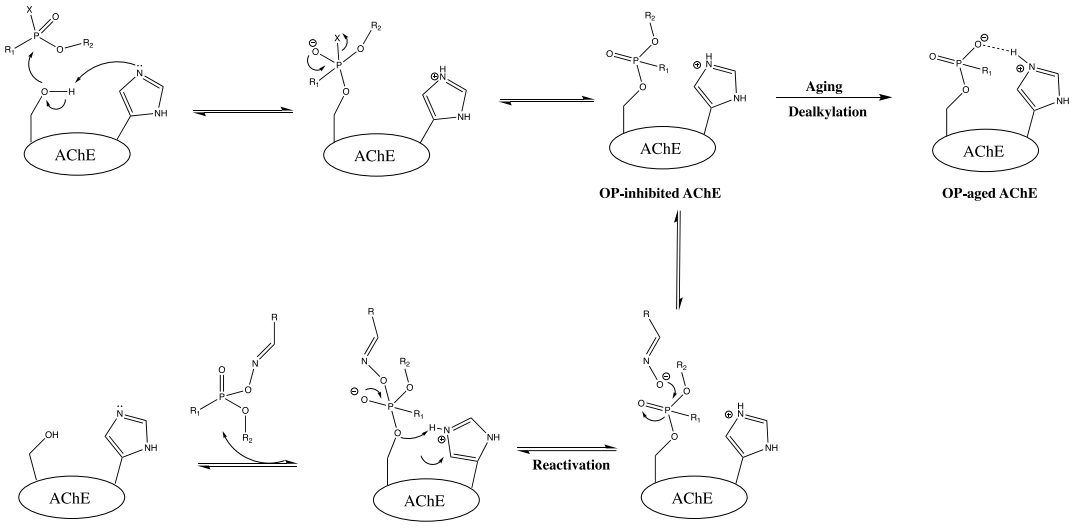

Figure 1.5 (Top) Mechanism of inhibition and aging. (Bottom) Mechanism of reactivation.

While a nucleophilic oxime is capable of reactivating AChE which has been inhibited by an OP, a process known as *aging* makes reactivation more difficult. Aging is a spontaneous process and occurs via *O*-dealkylation of the phosphylated S203 residue (**Figure 1.5**). Because the phosphylated serine's oxygen atom is now anionic, the phosphorus center is more electron rich and is resistant to nucleophilic attack by the negatively charged oximate form of the oxime reactivator.[16]

As each OP has a different structure, one might hypothesize that the aging rates for each OP are different. This hypothesis is correct, and the different aging rates can be vastly different (**Table 1.1**). For example, VR has an aging half-life of 139 hours while soman has an aging half-life of only 4 minutes.[17] Going forward, the aforementioned AChE-OP adduct, which has undergone *O*-dealkylation, will be referred to as the *aged* form of the enzyme. Restoration of the native AChE function to the aged form of the enzyme will be referred to as *resurrection*.[16]

OP	Aging half-time (h)
Soman (GD)	0.07
Sarin (GB)	3
Methyl Paraoxon	3.7
Cyclosarin (GF)	7
Tabun (GA)	19.2
Ethyl Paraoxon	31.5
VX	36.5
VR	138.6

Table 1.1 Aging half-times of various OPs

Although there has been active research into the reactivation and resurrection of AChE for nearly 70 years, only one oxime, pralidoxime chloride (2-PAM) has been approved by the US FDA for the reactivation of inhibited AChE (**Figure 1.6**). However, as the species has a permanent positive charge, the molecule is unable to effectively cross the blood-brain barrier (BBB) which limits the reactivation of OP-inhibited AChE in the brain. Currently, there are no FDA-approved treatments capable of resurrection. Indeed, until 2018, the aged form of AChE was considered recalcitrant to any recovery of activity.

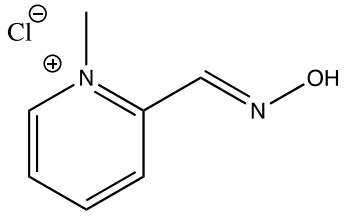

Pralidoxime Chloride (2-PAM)

Figure 1.6 Pralidoxime Chloride (2-PAM)

In 2018, our research group demonstrated the first molecules, referred to as quinone methide precursors (QMPs), that are capable of resurrection (**Figure 1.7**).[18] The QMP is capable of forming a quinone methide (QM) which are a known class of alkylating agents (**Figure 1.7**).[21] The QM can be trapped by the aged form of the enzyme, at which point the enzyme can undergo reactivation.

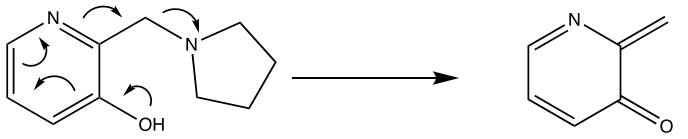

Quinone Methide Precurosr (QMP) **Quinone Methide (QM)**

Figure 1.7 Mechanism of QM formation on a model QMP

While the ability of a QMP to resurrect aged AChE is impressive, the QMP contains one more significant advantage over 2-PAM. Notably, the QMPs lack the permanent positive charge found in 2-PAM which should improve the ability of the QMP to cross the BBB to resurrect and reactivate AChE found in the brain.

The initial success of the QMP shown in **Figure 1.7** prompted a computational investigation into how the QMP entered and interacted with the active site of AChE. While the interactions between the QMP and AChE were modelled successfully, a frustrating complication quickly became apparent. While the QMP in **Figure 1.7** is shown to be in a neutral protonation state, one finds that the number of protonation states is equal to 2^x where x is equal to the number of titratable protons in a molecule. Molecular dynamics calculations have shown that the variation of the protonation state results in the QMP navigating to different sites within the enzyme (**Figure 1.8**). Distance maps (provided by Joseph Fernandez in our research group) provide a way to visualize these differences, by showing the proximity of different residues and the QMP. Consequently, we have hypothesized that the protonation state of a QMP at physiological pH may impact the ability of a QMP to resurrect aged AChE.

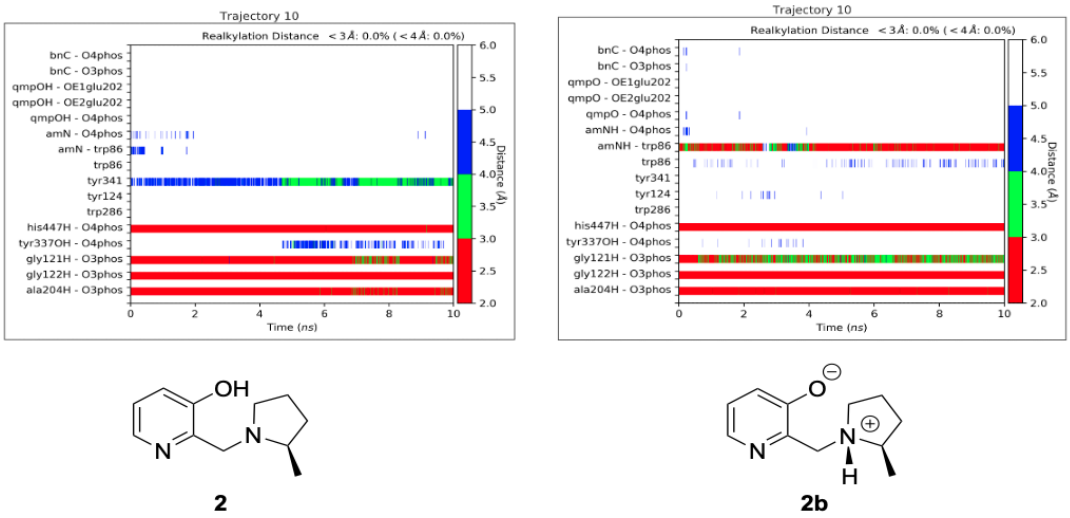

2

2b

Figure 1.8 Distance maps showing differences between certain atoms in the QMP and the active site of AChE. (Distance maps provided by Joseph Fernandez.)

Thus far, only countermeasures for individuals already exposed to an OP have been described. While most OP exposure occurs via either inhalation or dermal exposure of the OP, nerve agents and pesticides are water soluble. Consequently, an individual could experience a cholinergic crisis upon drinking OP-contaminated water.

In the event of a large-scale military attack, local water sources could be directly targeted for contamination with chemical agents. If portable water sources are not available, both military and civilian populations could be incapacitated. While there are devices for filtering dirt and other non-lethal contaminants from water, little work has been done to develop methods which could be used to remove a chemical agent from water.

Border et al. have noted this problem, and synthesized a molecular basket capable of encapsulating, and removing, OP analogues from an aqueous solution.[19] Border et al. have

since worked to develop and characterize new molecular baskets which could be derivatized to remove an authentic nerve agent from an aqueous solution.

The molecular baskets are quite large and the specific interactions between the basket and a guest are not well known. Additional information about how a guest binds within a basket could lead to developments of new baskets which are better able to sequester an OP species. Computational experiments to determine the orientation of small guests within a basket will be discussed in Chapter 2. Chapter 2 will also describe computational techniques to calculate NMR spectra and coupling constants which were used to corroborate experimental NMR observations.

The protonation state of model QMPs will be explored in Chapter 3 through the use of experimental and computational NMR and IR spectroscopic approaches.

References for Chapter 1

(1) Gunnell, D.; Eddleston, M.; Phillips, M.R.; Konradsen, F. The global distribution of fatal pesticide self-poisoning: Systematic review., *BMC Public Health,* 7, 357 (**2007**).

(2) Tucker, J. B. *War of Nerves*; Anchor, 2007.

(3) Franjesevic, A. J.; Sillart, S. B.; Beck, J. M.; Vyas, S.; Callam, C. S.; Hadad, C. M. Resurrection and Reactivation of Acetylcholinesterase and Butyrylcholinesterase., *Chem. Eur. J.,* **2018**, 1–36.

(4) Pitschmann, V. Overall View of Chemical and Biochemical Weapons, *Toxins*, **2014**, 6 (6): 1761–1784

(5) Central Intelligence Agency. Iraq's Chemical Warfare Program https://www.cia.gov/library/reports/general-reports-1/iraq_wmd_2004/chap5.html (accessed Feb 03, 2020).

(6) Stone, R. Chemical Martyrs, *Science,* **2018**, 359 (6371), 20–25.

(7) The White House. Government Assessment of the Syrian Government's Use of Chemical Weapons on August 21, 2013 https://www.whitehouse.gov/the-pressoffice/2013/08/30/government-assessment-syrian-government-s-use-chemicalweapons-august-21 (accessed Feb 03, 2020).

(8) The White House. United States Government Assessment of the Assad Regime's Chemical Weapons Use on April 13, 2018 https://whitehouse.gove/briefings-

statements/united-states-government-assessment-assad-regimes-chemical-weapons-use (accessed Feb 03, 2020)

(9) Eileen Ng. Malaysia charges two women in death of Kim Jong-nam. *The Globe and Mail*. https://web.archive.org/web/20170306034317/http://www.theglobeandmail.com/news/world/north-korean-diplomats-in-malaysia-seek-kim-jong-nams-body/article34157158/ (Accessed Feb 07, 2020)

(10) Kim Jong-nam death: suspect Siti Aisyah released after charge dropped *The Guardian* https://www.theguardian.com/world/2019/mar/11/kim-jong-nam-trial-siti-aisyah-released-after-charge-dropped (Accessed Feb 07, 2020)

(11) Asthana, A.; Roth, A.; Harding, L.; MacAskill, E. Russian Spy Poisoning: Theresa May Issues Ultimatum to Moscow. *The Guardian*. March 13, 2018. https://www.theguardian.com/uk-news/2018/mar/12/russia-highly-likely-to-be-behind-poisoning-of-spy-says-theresa-may (Accessed Feb 07, 2020)

(12) A, Harriet. Amesbury Incident Latest: Wiltshire Couple Were Exposed to Novichok Nerve Agent, Police Say. *The Independent, Independent Digital News and Media* July 4, 2018. www.independent.co.uk/news/uk/home-news/amesbury-poisoning-latest-novichock-metropolitan-police-neil-basu-professor-dame-sally-davies-a8431916.html (Accessed Feb 12, 2020)

(13) Summary Of The Report On Activities Carried Out In Support Of A Request For Technical Assistance By The United Kingdom Of Great Britain And Northern Ireland (Technical Assistance Visit (Tav) 02/18), OPCW, April 2018.

(14) Beck, J. M.; Hadad, C. M. Reaction Profiles of the Interaction between Sarin and Acetylcholinesterase and the S203C Mutant: Model Nucleophiles and QM/MM Potential Energy Surfaces, *Chem. Biol. Interact.,* **2010**, *187* (1–3), 220–224.

(15) Yanzi, Z.; Shenglong, W.; Yingkai, Z. Catalytic Reaction Mechanism of Acetylcholinesterase Determined by Born-Oppenheimer Ab Initio QM/MM Molecular Dynamics Simulations, *J. Phys. Chem. B.,* **2010**, *114, 26, 8817-8825.*

(16) Topczewski, J. J.; Quinn, D. M Kinetic Assessment of N-methyl-2-methoxypyridinium Species as Phosphate Anion Methylating Agents, *Org. Lett.,* **2013**, *15* (5), 1084–1087.

(17) Worek, F.; Thiermann, H. The Value of Novel Oximes for Treatment of Poisoning by Organophosphorus Compounds, *Pharmacol Ther.,* **2013,** 139, 249-259.

(18) Zhuang, Q.; Franjesevic, A. J.; Corrigan, T. S.; Coldren, W. H.; Dicken, R.; Sillart, S.; Deyong, A.; Yoshino, N.; Smith, J.; Fabry, S.; Fitzpatrick, K.; Blanton, T.G.; Joseph, J.; Yoder, R. J.; McElroy, C. A.; Ekici, Ö. D.; Callam, C. S.; Hadad, C. M. Demonstration of In Vitro Resurrection of Aged Acetylcholinesterase after Exposure to Organophosphorus Chemical Nerve Agents, *J. Med. Chem.,* **2018**, *61* (16), 7034–7042.

(19) Border. S. E.; Pavlovic. R. Z.; Zhiquan. L.; Badjic. D. J. Removal of Nerve Agent Simulants from Water Using Light Responsive Molecular Baskets, *J. Am. Chem. Soc.,* **2017**, *139* (51), 18496-18499

(20) Mercey, G.; Verdelet, T.; Renou, J.; Kliachyna, M.; Baati, R.; Nachon, F.; Jean, L.; Renard, P. Y. Reactivators of Acetylcholinesterase Inhibited by Organophosphorus Nerve Agents, *Acc. Chem. Res.,* **2012**, 45, 5, 756-766

(21) Valentin, C. D.; Freccero, M.; Zanaletti, Riccardo.; Sarzi-Amadè, M. o-Quinone Methide as Alkylating Agent of Nitrogen, Oxygen, and Sulfur Nucleophiles. The Role of H-Bonding and Solvent Effects on the Reactivity through a DFT Computational Study, *J. Am. Chem. Soc.*, **2001**, 123, 34, 8366-8377.

Chapter 2: Molecular Baskets

Supramolecular chemistry has been a burgeoning area of chemistry for over 50 years.[1] Over that time, a host of applications such as fluorescent sensors, drug carriers, and hydrometallurgy have been developed.[1] Although supramolecular chemistry has a large number of applications, at its core, supramolecular chemistry can be described as the study of molecular recognition and high-order assemblies formed by noncovalent interactions.[2] Commonly, these noncovalent interactions are described as interactions between both a host and a guest, where the host encapsulates the guest.

A plethora of examples in the literature show hosts which have been specifically tailored to encapsulate a particular set of guests. An early example of the tailoring of a host to encapsulate a guest can be seen in crown ethers. In the gas phase, two simple crown ethers, 18-crown-6 and 15-crown-5 (**Figure 2.1**) show remarkable affinities for the sodium and lithium cations, respectively.[3] 15-Crown-5, being the smaller crown ether, prefers to bind the smaller lithium cation over the larger sodium cation with a 100:10 ratio, while the larger 18-crown-6 has a small preference for the sodium cation over the lithium cation with a 100:40 ratio.[3]

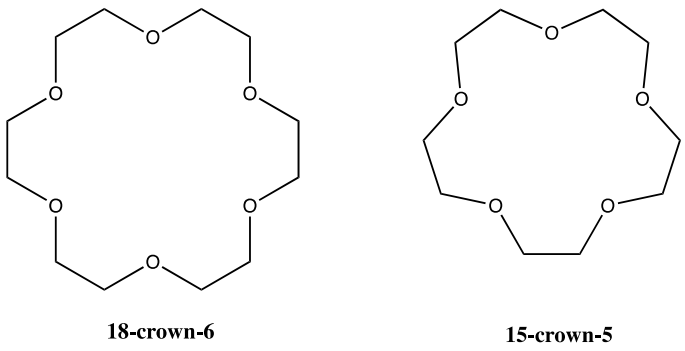

Figure 2.1 Chemical structures of 18-crown-6 and 15-crown-5

In the case of the crown ethers, the encapsulation of a cation within the ether is easy to visualize. Additionally, the manipulation of the crown ether size, allows for the easy sequestration of a variety of cations.[3] While the use of crown ethers as hosts is limited, researchers have developed complex host systems capable of sequestering a variety of novel guests. Notably, Border et al. have reported the synthesis of a host capable of sequestering and subsequently removing a G-type nerve agent mimic from aqueous solution.[4] Although Border et al. successfully developed a system for removing several small G nerve agent mimics from solution, the G agents are, in comparison to V agents and Novichoks, small. While the researchers did not test a larger V agent or Novichok agent mimic, one might reason that the larger size of these mimics would make them less likely to be encapsulated in the aforementioned basket system.

Pavlovic et al. have continued to develop and characterize new molecular baskets with larger internal volumes.[5] While the new basket developed by Pavlovic et al. was not explicitly made for the encapsulation of a larger V or Novichok agent mimic, one might reason that the larger size of this system might lend itself to the encapsulation of such mimics. Interestingly, the researchers noticed that the lid of the new basket was capable of rapid twisting, resulting in two distinct diastereomeric baskets (**Figure 2.2**), which will subsequently be referred to as M-1(-) and M-1(+).[5] To determine whether each diastereomer had the same preferences for binding a host, we explored the binding interactions of carbon tetrachloride and carbon tetrabromide via a combination of computational and experimental methods.

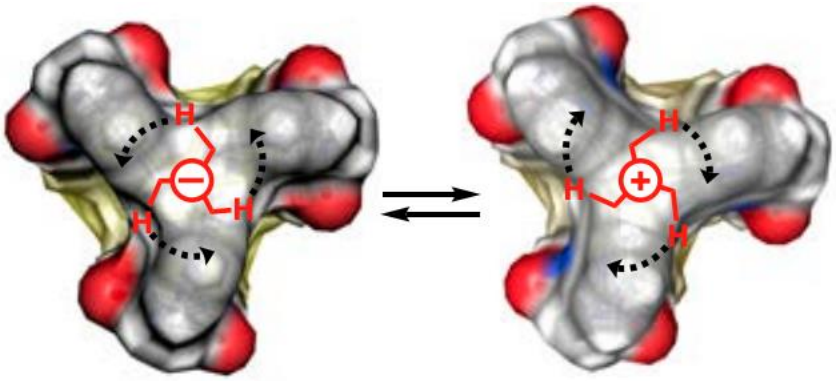

Figure 2.2 Depiction of the helical chirality of the basket lid

The binding events between a guest and a host can be probed via UV-vis, IR, and NMR as the introduction of a guest into the host molecule changes the characteristics of the parent host molecule.[6] A comparison between experimental and calculated spectra can then be used to provide insight into the binding orientation of the guest within the host. While the binding orientation can be determined via a variety of computational and analytical techniques, the binding affinity between a host and guest molecule can also be determined. In particular, both NMR and UV-vis can provide information about a host and guests binding strengths. NMR can be used for moderate binding events on the order of K_a = 1–10 M^{-1} while UV-vis can be used for larger values on the order of $K_a = 10^3 – 10^7\ M^{-1}$.[6]

To monitor the binding event of a host and guest via NMR, the shifts of the native host and guest need to be known. Upon addition of the guest, the new host-guest complex will have new chemical shifts. Comparison of the intensities of the host and host-guest complex's resonances can provide insights into the concentrations of the host-guest complex. One should note that the equilibrium concentrations can only be obtained via NMR for processes which are

slow on the NMR timescale. As the aforementioned diastereomer interconversion is fast on the NMR timescale, experimental NMR spectra were taken at approximately 180 K.[5]

While the NMR shifts for a parent complex can be trivial to obtain and characterize, the NMR shifts for species with similar chemical shifts can be complex. Fortunately, several different methods for the *in-silico* determination of chemical shifts and coupling constants are easily computed via the Gaussian 16 program (G16).[7] Subsequently, a comparison of the *in-silico* NMR spectra from each species can be compared to experimentally obtained results in order to elucidate the chemical shifts of each species. Fascinatingly, *in silico* NMR calculations are so accurate, that several natural product syntheses have been revised due to poor match between the shifts of the proposed structure and the calculated shifts.[8, 9]

Although the Gaussian suite offers several ways to calculate NMR shielding tensors, such as the Continuous Set of Gauge Transformations (CSGT)[10,11] and the Gauge-Independent Atomic Orbital (GIAO)[12-15] method, only the GIAO method will be used for this work. Likewise, unless otherwise noted, all geometry optimizations were carried out in the gas phase as solvent effects were not considered. All calculations were performed with both the B3LYP[16-18] as well as the M06-2X[18-19] density functionals. The 6-31+G(d)[20-24] basis set was used for the atoms C, N, O, H, and Cl. The larger 6-311+G(2d)[25-29] basis set was used for Br. Additionally, while vibrational frequency analyses were not carried out on the optimized structures, the optimized structures were compared to and found to be similar to an available crystal structure.

Analysis of the resultant optimized energies (**Table 2.1**) showed that the M-1(-) diastereomer was predicted to be higher in concentration. This finding directly contradicts the

experimental NMR data obtained by Radoslav in which the M-1(+) species was found to be higher in concentration. One should note that the energies shown in **Table 2.1** indicate an approximate 0.9 kcal/mol difference in energy between the two species. Fascinatingly, the M–1(–)⊂CX_4 species was found to be lower in energy for both CBr_4 and CCl_4 (**Table 2.2**). However, it should again be noted that the energy difference between the two diastereomers is less than 1.5 kcal/mol. Experimental NMR spectra corroborate that the M–1(–)⊂CX_4 diastereomer is the most stable species.

Species	**Theory (6-31+G* for C, N, O, H)**	**Absolute electronic energy (Hartrees)**	**Relative electronic energy (kcal/mol)**
M-1(+)	B3LYP	-3723.61379479	0.91
	M06-2X	-3722.17693905	0.92
M-1(-)	B3LYP	-3723.61524342	0.00
	M06-2X	-3722.17840431	0.00

Table 2.1 Relative and absolute energies of the M-1(-)/M-1(+) diastereomers.

Species	Theory (6-31+G* for C, N, O, H, and Cl 6-311+G(2d) for Br)	Absolute electronic energy (Hartrees)	Relative electronic energy (kcal/mol)
M–1(+)⊂CCl_4	B3LYP	-5602.47166579	0.64
	M06-2X	-5600.92300646	1.48
M–1(-)⊂CCl_4	B3LYP	-5602.47268954	0.00
	M06-2x	-5600.92537130	0.00
M–1(+)⊂CBr_4	B3LYP	-14058.2614840	0.45
	M06-2X	-14056.9485237	0.71
M–1(-)⊂CBr_4	B3LYP	-14058.2622090	0.00
	M06-2X	-14056.9496610	0.00

Table 2.2 Absolute electronic energies of M–1(+)/M–1(-)⊂CX4 diastereomers with relative energies in kcal/mol.

While the initial assignment of M–1(–) and M–1(+) were made from experimental ^{1}H NMR, we wanted to computationally corroborate the proton assignments. To begin the ^{1}H NMR calculations, tetramethylsilane (TMS) was optimized with both the B3LYP and M06-2X density functionals, along with the 6-31+G* basis set. A vibrational frequency analysis was also performed on TMS to ensure that the optimized geometry was a true minimum on the

potential energy surface. All subsequent ^{1}H chemical shifts of M–1(–) and M–1(+) will be referenced to the TMS shifts calculated with the appropriate density functional.

The ground-state geometries referenced in **Table 2.1** were subjected to single-point NMR calculations with both the M06-2X and B3LYP density functionals using the aforementioned GIAO method. **Figure 2.3** shows the labeled position of each of the calculated protons for the M-1(-) diastereomer. The protons in the M-1(+) diastereomer are labeled in a similar manner. The chemical shifts of all calculated protons are shown in **Table 2.3**. Interestingly, in the un-complexed M-1(+)/M-1(-) diastereomers, the B3LYP density functional provided calculated values within approximately 0.20 ppm for all calculated protons, while M06-2X method predicted values that often varied by more than 0.75 ppm. Additionally, upon analysis of the M-1(+)/M-1(-)$\subset CX_4$ complexed species, both B3LYP and M06-2X predict the same relative trends of upfield and downfield shifts when comparing the M-1(+)/M-1(-) diastereomers and the M-1(+)/M-1(-)$\subset CX_4$ species.

While the calculated NMR shifts agreed well with experimental spectra, analysis of the computed data revealed one other interesting caveat. Upon optimization of the M-1(+)/M-1(-)$\subset CX_4$ species, the CX_4 appeared to form a stabilizing halogen – π bond with the floor of the basket. The M-1(-)$\subset CX_4$ species additionally formed three stabilizing C- H···X interactions which were absent in the M-1(+)$\subset CX_4$ basket.[5] Consequently, future works should investigate the use of the M-1(+)/M-1(-) species and their ability to sequester both V-agents as well as Novichok agents via favorable lone pair – π bonds as well as π- π interactions. If the M-1(+)/M-1(-) system

is used in the future, researchers should first attempt to correlate experimental data to computational data for the M-1(-)⊂Guest system.

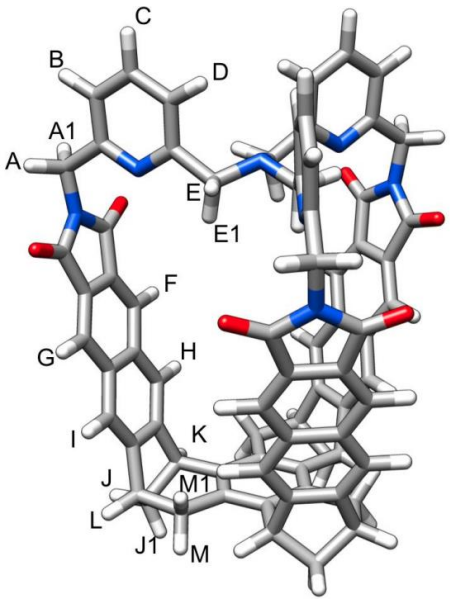

Figure 2.3 The M-1(-) diastereomer showing the positions of all calculated protons.

Summary of ^{1}H NMR Shifts						
	NMR Minor	NMR Major	NMR Major	NMR Minor	NMR Major	NMR Minor
Proton	M-1(+)	M-1(-)	M-1(+)⊂ CCl_4	M-1(-)⊂ CCl_4	M-1(+)⊂ CBr_4	M-1(-)⊂ CBr_4
A						
Experiment	4.95	4.73	4.80	4.75	4.99	4.76
B3LYP	4.84 ± 0.01	4.59 ± 0.03	4.68 ± 0.02	4.51 ± 0.03	4.98 ± 0.04	4.46 ± 0.02
M06-2X	4.99 ± 0.01	4.76 ± 0.09	4.95 ± 0.03	4.76 ± 0.03	5.05 ± 0.02	4.78 ± 0.06

Table 2.3 All experimental and calculated proton shifts for the M-1(+)/M-1(-) and the shifts associated for each diastereomer with an encapsulated guest.

A1						
Experiment	4.79	4.85	4.94	4.84	4.79	4.86
B3LYP	4.81 ± 0.02	4.80 ± 0.03	4.74 ± 0.01	4.82 ± 0.01	4.57 ± 0.01	4.83 ± 0.01
M06-2X	4.99 ± 0.01	4.95 ± 0.04	5.04 ± 0.05	4.93 ± 0.02	4.94 ± 0.02	4.91 ± 0.01
B						
Experiment	7.09	7.09	7.09	7.11	7.13	7.13
B3LYP	6.94 ± 0.01	6.91 ± 0.03	6.86 ± 0.01	6.88 ± 0.02	6.88 ± 0.02	6.89 ± 0.01
M06-2X	7.71 ± 0.05	7.69 ± 0.02	7.72 ± 0.04	7.68 ± 0.08	7.75 ± 0.05	7.69 ± 0.05
C						
Experiment	7.55	7.55	7.57	7.57	7.62	7.62
B3LYP	7.58 ± 0.04	7.53 ± 0.02	7.45 ± 0.03	7.51 ± 0.02	7.57 ± 0.02	7.52 ± 0.02
M06-2X	8.34 ± 0.02	8.23 ± 0.04	8.23 ± 0.04	8.24 ± 0.08	8.28 ± 0.01	8.31 ± 0.04
D						
Experiment	7.37	7.40	7.36	7.43	7.50	7.54
B3LYP	7.46 ± 0.02	7.58 ± 0.02	7.16 ± 0.03	7.56 ± 0.01	7.59 ± 0.02	7.54 ± 0.01
M06-2X	8.17 ± 0.01	8.57 ± 0.05	8.03 ± 0.04	8.54 ± 0.02	8.42 ± 0.07	8.63 ± 0.02
E						
Experiment	3.19	3.43	3.17	3.36	3.39	3.51
B3LYP	3.15 ± 0.01	3.31 ± 0.02	2.97 ± 0.02	3.40 ± 0.02	3.53 ± 0.01	3.57 ± 0.01
M06-2X	2.99 ± 0.03	3.36 ± 0.03	3.06 ± 0.01	3.33 ± 0.02	3.16 ± 0.03	3.43 ± 0.01
E1						
Experiment	2.28	2.34	2.53	2.60	2.99	3.04
B3LYP	2.47 ± 0.02	2.52 ± 0.02	2.66 ± 0.05	2.91 ± 0.02	3.35 ± 0.02	3.35 ± 0.04
M06-2X	2.40 ± 0.02	2.49 ± 0.06	2.88 ± 0.01	3.01 ± 0.04	3.37 ± 0.04	3.47 ± 0.08
F						
Experiment	8.04	8.04	8.01	8.07	8.10	8.10
B3LYP	7.81 ± 0.02	7.87 ± 0.03	7.87 ± 0.02	7.90 ± 0.05	7.89 ± 0.03	8.01 ± 0.04

M06-2X	8.57 ± 0.02	8.64 ± 0.03	8.60 ± 0.09	8.72 ± 0.01	8.78 ± 0.04	8.83 ± 0.04
G						
Experiment	8.22	8.15	8.17	8.09	8.16	8.15
B3LYP	8.10 ± 0.04	8.03 ± 0.03	8.03 ± 0.03	7.94 ± 0.05	8.08 ± 0.02	7.94 ± 0.06
M06-2X	8.85 ± 0.06	8.74 ± 0.05	8.73 ± 0.16	8.63 ± 0.13	8.77 ± 0.03	8.67 ± 0.04
H						
Experiment	7.54	7.54	7.50	7.47	7.60	7.60
B3LYP	7.48 ± 0.06	7.53 ± 0.08	7.50 ± 0.04	7.50 ± 0.07	7.52 ± 0.02	7.59 ± 0.09
M06-2X	8.26 ± 0.01	8.30 ± 0.09	8.27 ± 0.02	8.43 ± 0.02	8.29 ± 0.01	8.29 ± 0.06
I						
Experiment	7.97	7.94	7.93	7.91	7.99	7.99
B3LYP	7.90 ± 0.02	7.82 ± 0.03	7.85 ± 0.02	7.74 ± 0.16	7.92 ± 0.03	7.83 ± 0.15
M06-2X	8.71 ± 0.01	8.66 ± 0.11	8.7 ± 0.07	8.67 ± 0.10	8.70 ± 0.06	8.69 ± 0.08
J						
Experiment	2.51	2.51	2.50	2.50	2.53	2.53
B3LYP	2.58 ± 0.03	2.56 ± 0.09	2.52 ± 0.06	2.64 ± 0.09	2.64 ± 0.01	2.61 ± 0.02
M06-2X	2.60 ± 0.19	2.63 ± 0.17	2.57 ± 0.14	2.55 ± 0.12	2.70 ± 0.10	2.69 ± 0.13
J1						
Experiment	2.05	2.05	2.06	2.06	2.08	2.08
B3LYP	2.19 ± 0.05	2.23 ± 0.05	2.13 ± 0.05	2.24 ± 0.05	2.16 ± 0.06	2.16 ± 0.03
M06-2X	2.24 ± 0.07	2.20 ± 0.10	2.23 ± 0.09	2.22 ± 0.03	2.23 ± 0.10	2.20 ± 0.12
K						
Experiment	4.36	4.36	4.34	4.34	4.33	4.33
B3LYP	4.15 ± 0.01	4.18 ± 0.01	4.20 ± 0.05	4.25 ± 0.03	4.19 ± 0.02	4.27 ± 0.04
M06-2X	4.38 ± 0.07	4.25 ± 0.18	4.57 ± 0.22	4.52 ± 0.12	4.31 ± 0.19	4.31 ± 0.22
L						
Experiment	3.79	3.79	3.78	3.78	3.78	3.78
B3LYP	3.54 ±	3.57 ±	3.55 ±	3.58 ±	3.56 ±	3.57 ±

	0.01	0.06	0.03	0.02	0.03	0.04
M06-2X	3.48 ± 0.14	3.54 ± 0.12	3.55 ± 0.08	3.53 ± 0.15	3.49 ± 0.03	3.53 ± 0.04
M						
Experiment	3.61	3.61	3.56	3.56	3.59	3.59
B3LYP	3.51 ± 0.01	3.54 ± 0.03	3.51 ± 0.03	3.62 ± 0.04	3.48 ± 0.01	3.56 ± 0.07
M06-2X	3.41 ± 0.29	3.29 ± 0.15	3.44 ± 0.05	3.58 ± 0.25	3.36 ± 0.14	3.40 ± 0.17
M1						
Experiment	2.93	2.93	2.95	2.95	2.98	2.98
B3LYP	3.29 ± 0.05	3.28 ± 0.05	3.23 ± 0.04	3.21 ± 0.04	3.22 ± 0.03	3.20 ± 0.06
M06-2X	3.56 ± 0.04	3.53 ± 0.06	3.70 ± 0.13	3.81 ± 0.08	3.59 ± 0.07	3.63 ± 0.07

References for Chapter 2

(1) Kolesnichenko. I. V.; Anslyn. E. V. Practical Applications of Supramolecular Chemistry, *Chem. Soc. Rev.* **2017**, 46, 2385-2390

(2) You, L.; Zha, D.; Anslyn, E. V. Recent Advances in Supramolecular Analytical Chemistry Using Optical Sensing, *Chem. Rev.* **2015**, 115, 15, 7840–7892.

(3) Maleknia, S.; Brodbelt, J. Gas-phase Selectivities of Crown Ethers for Alkali Metal Complexation, *J. Am. Chem. Soc.* **1992**, 114, 4295–4298.

(4) Border, S. E.; Pavlovic, R. Z.; Zhiquan, L.; Badjic, J. D. Removal of Nerve Agent Simulants from Water Using Light Responsive Molecular Baskets *J. Am. Chem. Soc*. **2017**, 139, 18496−18499

(5) Pavlovic, R. Z.; Lei, Z.; Gueney, M.; Lalisse, R. F.; Hopf, R. G.; Gallucci, J.; Moore, C.; Xie, H.; Hadad, C. M.; Badjic, J. D. Multivalent C−H···Cl/Br−C Interactions Directing the Resolution of Dynamic and Twisted Capsules, *Chem. Eur. J.,* **2019**, 25, 13124-13130.

(6) Li, Y.; Vander Griend, D. A.; Flood, A. H. Modelling Triazolophane-halide Binding Equilibria Using Sivvu Analysis of UV-vis Titration Data Recorded Under Medium Binding Conditions, *Supramolec. Chem.* **2009**, 21, 111-117

(7) Frisch, M. J.; Trucks, G. W.; Schlegel, H. B.; Scuseria, G. E.; Robb, M. A.; Cheeseman, J. R.; Scalmani, G.; Barone, V.; Petersson, G. A.; Nakatsuji, H.; Li, X.; Caricato, M.; Marenich, A. V.; Bloino, J.; Janesko, B. G.; Gomperts, R.; Mennucci, B.; Hratchian, H. P.; Ortiz, J. V.; Izmaylov, A. F.; Sonnenberg, J. L.; Williams-Young, D.; Ding, F.;

Lipparini, F.; Egidi, F.; Goings, J.; Peng, B.; Petrone, A.; Henderson, T.; Ranasinghe, D.; Zakrzewski, V. G.; Gao, J.; Rega, N.; Zheng, G.; Liang, W.; Hada, M.; Ehara, M.; Toyota, K.; Fukuda, R.; Hasegawa, J.; Ishida, M.; Nakajima, T.; Honda, Y.; Kitao, O.; Nakai, H.; Vreven, T.; Throssell, K.; Montgomery, J. A., Jr.; Peralta, J. E.; Ogliaro, F.; Bearpark, M. J.; Heyd, J. J.; Brothers, E. N.; Kudin, K. N.; Staroverov, V. N.; Keith, T. A.; Kobayashi, R.; Normand, J.; Raghavachari, K.; Rendell, A. P.; Burant, J. C.; Iyengar, S. S.; Tomasi, J.; Cossi, M.; Millam, J. M.; Klene, M.; Adamo, C.; Cammi, R.; Ochterski, J. W.; Martin, R. L.; Morokuma, K.; Farkas, O.; Foresman, J. B.; Fox, D. J. Gaussian 16, Rev. A. 03 Gaussian, Inc., Wallingford CT, 2016.

(8) Chhetri. B. K.; Lavoie. S.; Sweeney-Jones. A. M.; Kubanek. J. Recent Trends in the Structural Revision of Natural Products*, Nat. Prod. Rep.*, **2018**, 35, 1015-1015.

(9) Chhetri. B. K.; Lavoie. S.; Sweeney-Jones. A. M.; Kubanek. J. Recent Trends in the Structural Revision of Natural Products, *Nat. Prod. Rep.*, **2018**, 35, 514-531.

(10) Keith. T. A.; Bader. R. F. W. Calculation of Magnetic Response Properties Using Atoms in Molecules, *Chem. Phys. Lett.* **1992**, 194, 1-8.

(11) Keith, T. A.; Bader, R. F. W. Calculation of Magnetic Response Properties Using a Continuous Set of Gauge Transformations, *Chem. Phys. Lett.* **1993**, 210, 223-31.

(12) McWeeny, R. Perturbation Theory for the Fock-Dirac Density Matrix, *Phys. Rev.* **1962**, 126, 1028–1034.

(13) Wolinski, K.; Hinton, J. F.; Pulay, P. Efficient Implementation of the Gauge-independent Atomic Orbital Method for NMR Chemical Shift Calculations, *J. Am. Chem. Soc.* **1990**, 112, 8251–8260.

(14) Ditchfield, R. Self-consistent Perturbation Theory of Diamagnetism, *Mol. Phys.* **1974**, 27, 789–807.

(15) Cheeseman, J. R. A Comparison of Models for Calculating Nuclear Magnetic Resonance Shielding Tensors, *J. Chem. Phys*. **1996**, 104, 5497–5509.

(16) Becke, A. D. Density-functional Thermochemistry. III. The Role of Exact Change, *J. Chem. Phys.* **1993**, 98, 5648–5652.

(17) Kim, K.; Jordan, K. D. Comparison of Density Functional and MP2 Calculations on the Water Monomer and Dimer, *J. Phys. Chem*. **1994**, 98, 10089–10094.

(18) Stephens, P. J.; Devlin, F. J.; Chabalowski, C. F.; Frisch, M. J. Ab Initio Calculation of Vibrational Absorption and Circular Dichroism Spectra Using Density Functional Force Fields, *J. Phys. Chem.* **1994**, 98, 11623–11627.

(19) Zhao, Y.; Truhlar, D. G. Density Functionals with Broad Applicability in Chemistry, *Acc. Chem. Res.* **2008**, 41, 157–167.

(20) Ditchfield, R.; Hehre, W. J.; Pople, J. A. Self-Consistent Molecular-Orbital Methods. IX. An Extended Gaussian-Type Basis for Molecular-Orbital Studies of Organic Molecules, *J. Chem. Phys.* **1971**, 54, 724–728.

(21) Hehre, W. J.; Ditchfield, K.; Pople, J. A. Self-Consistent Molecular Orbital Methods. XIV. An Extended Gaussian-Type Basis for Molecular Obrital Studies of Organic Molecules. Inclusion of Second Row Elements, *J. Chem. Phys.* **1972**, 56, 2257–2261.

(22) Hariharan, P. C.; Pople, J. A. Accuracy of AHn Equilibrium Geometries by Single Determinant Molecular Orbital Theory, *Mol. Phys.* **1974**, 27, 209–214.

(23) Gordon, M. S. The Isomers of Silacyclopropane, *Chem. Phys. Lett*. **1980**, 76, 163–168.

(24) Hariharan, P. C.; Pople, J. A. The Influence of Polarization Functions on Molecular Orbital Hydrogenation Energy, *Theor. Chim. Acta.* **1973**, 28, 213–222.

(25) McLean, A. D.; Chandler, G. S. Contracted Gaussian Basis Sets for Molecular Calculations. I. Second Row Atoms, Z=11-18, *J. Chem. Phys.* **1980**, 72, 5639–5648.

(26) Krishnan, R.; Binkley, J. S.; Seeger, R.; Pople, J. A. Self-consistent Molecular Orbital Methods. XX. A Basis Set for Correlated Wave Functions, *J. Chem. Phys.* **1980**, 72, 650–654.

(27) Hay, P. J. Gaussian Basis Sets for Molecular Calculations. The Representation of 3d Orbitals in Transition-metal Atoms, *J. Chem. Phys.* **1977**, 66, 4377–4384.

(28) Raghavachari, K.; Trucks, G. W. Highly Correlated Systems. Excitation Energies of First Row Transition Metals Sc-Cu, *J. Chem. Phys.* **1989**, 91, 1062–1065.

(29) Wachters, A. J. H. Gaussian Basis Sets for Molecular Wavefunctions Containing Third-Row Atoms, *J. Chem. Phys.* **1970**, 52, 1033–1036.

Chapter 3: A Study of the Protonation States of Novel Therapeutics for the Resurrection of Organophosphorus-Aged Acetylcholinesterase

Investigations into the function of acetylcholinesterase (AChE) have long been of interest. As a result of these long-standing investigations, the function of native AChE is well understood.[1,2] However, upon inhibition of AChE by an organophosphorus (OP) nerve agent, the enzyme's native function is inhibited (**Figure 1.5**). Left untreated and after exposure to a sufficient dose, an individual who has been exposed to an OP will experience a cholinergic crisis, often leading to death.

While treatments for OP exposure exist, the treatments suffer from several limitations. Notably, current FDA treatments are incapable of restoring function to AChE which has undergone aging (**Figure 1.5**). Although no current FDA treatments are capable of restoring function to aged AChE, we have recently reported novel quinone methide precursors (QMPs), functionalized with amine leaving groups, and these novel frameworks serve to both resurrect OP-aged and reactivate OP-inhibited AChE.[3] Our group has continued to investigate QMPs and their ability to resurrect aged and reactivate inhibited AChE. During our investigation into what characteristics lead to favorable improvements in QMPs, we evaluated structure-activity relationships (SAR) to see which components can be used to build the best and most efficacious QMP. While novel QMPs, predicted by the SAR study, have outperformed their first-generation counterparts, we have hypothesized that the protonation state of our QMP may also need to be optimized.

This chapter will explore the protonation states of several different species based on five core frameworks modified with a variety of amine leaving groups. For consistency, the alcohol present on each pyridine framework will be assigned to the 3-position while the pyridine nitrogen will be assigned to the 1-position. Of these five frameworks, three correspond to the pyridin-3-ol, 5-methoxy-pyridin-3-ol, and 6-methyl-pyridin-3-ol frameworks shown in **Figure 3.1** to **Figure 3.3**, respectively. The last two frameworks correspond to the 5-fluoro-pyridin-3-ol framework, which will be divided into two distinct frameworks depending on whether the amine leaving group is found at either the 2- or the 6-position, as shown in **Figure 3.4** and **Figure 3.5**, respectively. The potential amine leaving groups (**A** through **F**) for each core framework are illustrated in **Figure 3.6**. Henceforth, each framework will be denoted by the associated compound number appended by the letter referencing the correct amine leaving group; for example, compound **3.3B** would refer to the 6-methyl-pyridin-3-ol framework with the diethylamine leaving group.

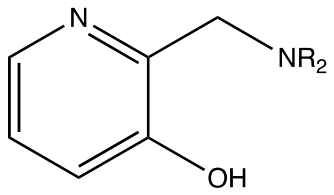

Figure 3.1 The pyridin-3-ol framework (**3.1** family)

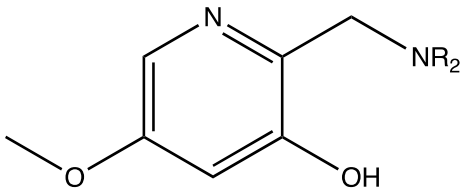

Figure 3.2 The 5-methoxy-pyridin-3-ol framework (**3.2** family)

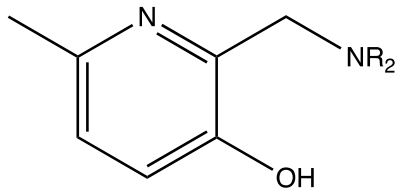

Figure 3.3 The 6-methyl-pyridin-3-ol framework (**3.3** family)

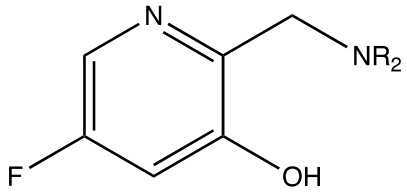

Figure 3.4 The 5-fluoro-pyridin-3-ol framework with the amine leaving group at the 2-position (**3.4** family).

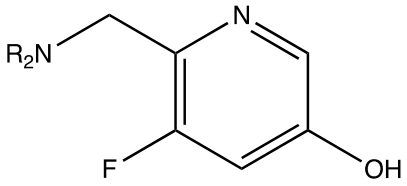

Figure 3.5 The 5-fluoro-pyridin-3-ol framework with the amine leaving group at the 6-position (**3.5** family).

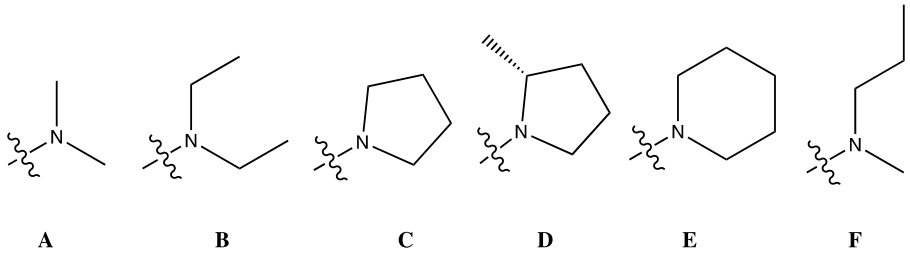

Figure 3.6 The referenced amine leaving groups for Figures 3.1 through 3.5.

Initial attempts by Ola Nosseir, a graduate student in our laboratory, to determine the protonation state of our compounds focused only on computational approaches. Nosseir used the EPIK[4,5] program to predict the protonation state for a variety of our QMP frameworks (

Figure 3.8) at different confidence intervals. Nosseir created a naming scheme to denote the different protonation states generated by EPIK. To avoid ambiguity with the amine leaving groups, the protonation state will be appended only as a lowercase. An illustration of the protonation states for compound **3.2B** is shown in **Figure 3.7**, denoting the involvement of the pyridinium (**p**), the aminium (**a**) and various zwitterion (**z**) options. At various pH values, these eight (8) different protonation states can be present. The **b** protonation state has a net +2 charge, while **a**, **zpa** and **p** possess a net +1 charge. For the net neutral states, **za**, **zp** and **n** are possible, and **d** has a net –1 charge. Consequently, **3.2B-za** would refer to the zwitter aminium protonation state for the 5-methoxy-pyridin-3-ol species with the diethylamine leaving group.

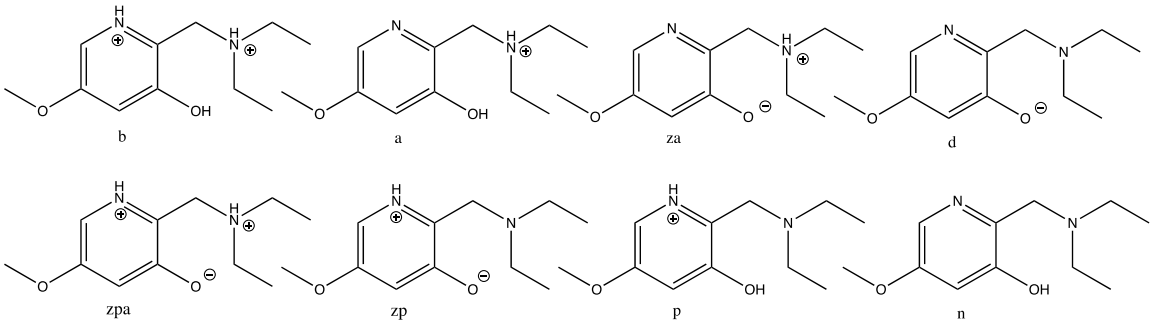

Figure 3.7 An illustration of the protonation states for compound **3.2B**.

While EPIK can predict protonation states for our compounds, the results were often determined to be a mix of many different protonation states of the molecule (

Figure 3.8). Consequently, we wished to generate experimental data which could corroborate our computational assignments as well as to investigate additional methods which may correlate with our efficacy data. Essentially, we sought to understand if the protonation state and its preference correlated with the efficacy of resurrection, thereby assisting our team in understanding the critical features for optimal drug design.

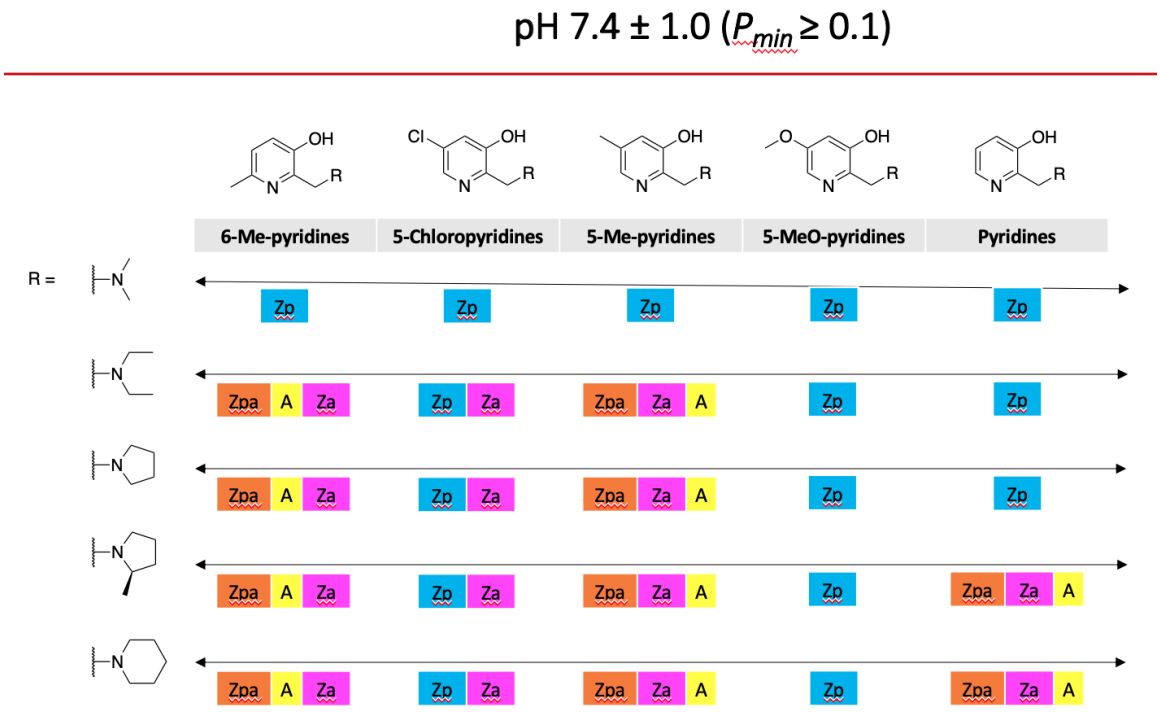

Figure 3.8 Protonation state data for a variety of QMP frameworks with various amine leaving groups at physiological pH (7.4), using a minimum probability of 0.1, as generated by Ola Nosseir.

Conveniently, samples with varying pH ranges can be examined via nuclear magnetic resonance (NMR). As the chemical shift of a nucleus depends on its chemical environment, a change in the protonation state of neighboring acidic protons results in a change in neighboring

proton's chemicals shifts, and possibly their coupling constants to other nuclei. As the deprotonation event results in a negative charge, the proton signals would shift upfield (**Figure 3.9**).

For these NMR spectra, most samples were prepared by diluting a stock solution of the QMP in water to create approximately 20 unique 1 mM samples in water. Samples **3.1**, **3.1A**, **3.1C**, **3.2** and **3.2B** were instead diluted to 1 mM using a 40 mM phosphate buffer in water. The final volume for all prepared samples was approximately 500 µL. Each unique sample was titrated with HCl or NaOH such that the 20 samples of a single compound spanned a pH range of approximately 1 – 12. After the pH titration, each sample was diluted with 50 µL of D_2O to give a final H_2O:D_2O ratio of approximately 90:10 and a final QMP concentration of approximately 900 µM. Any addition of D_2O to a sample had a marginal difference on the pH; for example, a sample with an initial pH of 11.96 was lowered to a pH of 11.91 when D_2O was added.

A 1-D ^{1}H NMR spectra was then obtained on a 400 MHz Avance Neo NMR from Bruker. Solvent suppression was performed utilizing 1D excitation sculpting with the zgesgp pulse sequence with an O1P set to 4.7 ppm. Spectra were obtained with 64 scans with a delay of one second between pulses. Each spectrum was obtained over a range of –11.67 to 21 ppm. Auto shimming was done via the IconNMR software program. While the excitation sculpting successfully suppressed the ^{1}H NMR peak from water, the suppression also severely impacted the analysis of the benzylic proton signals. At low pH, the benzylic proton signals were absent as

the water suppression reduced the benzylic signals of the QMP. As the pH of the solution increased, the benzylic signals began to grow in.

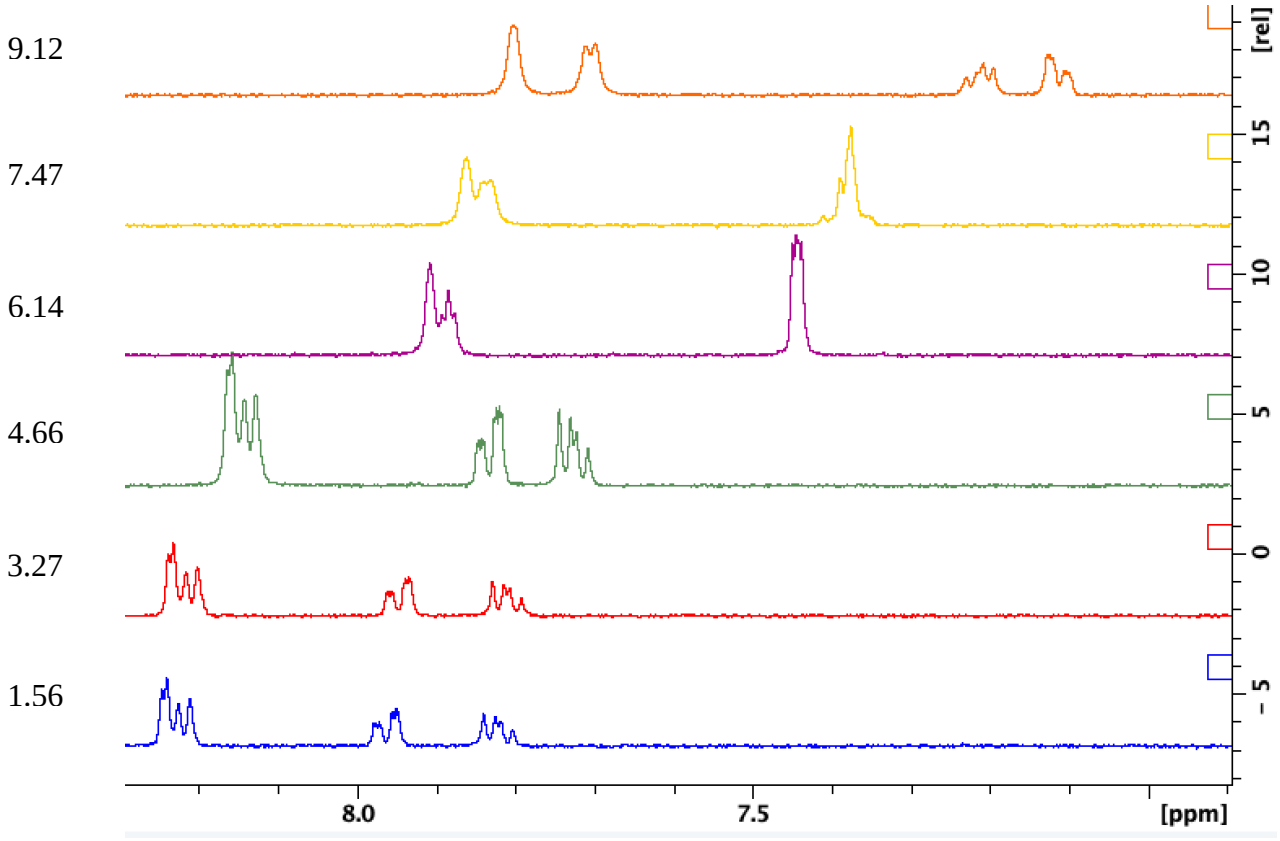

Figure 3.9 Subset of variable pH titration data for pyridin-3-ol, **3.1**. pH values for each NMR spectra are shown on the left.

By plotting the chemical shift vs the pH for each proton in each molecule, one obtains a graph with several sigmoidal curves.[6] Compound **3.1** (pyridin-3-ol) has only a few protonation states (+1: **p**; neutral: **n** and **zp**; –1: **d**), but this will be used as the first prototypical example. Each proton for **3.1** has been labeled, as in

Figure 3.10. Moreover, **Figure 3.10** also illustrates the conversion of the protonated pyridinium form (**3.1-p**) to the neutral form (**3.1-n**) and then conversion of **3.1-n** to the deprotonated form (**3.1-d**).

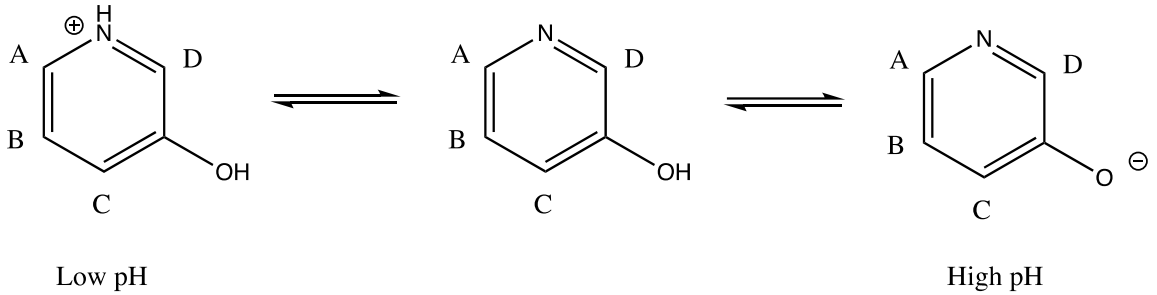

Figure 3.10 Species **3.1** with labeled protons illustrating multiple protonation states.

An example of the raw titration data for protons A and B (H on C6 and C5 respectively) of **3.1** are shown in **Figure 3.11**. The inflection point of these sigmoidal curves represents the pK_a for a titratable proton.[6] Analysis of **Figure 3.11** (right) indicated that **3.1** had two titratable protons with pK_a values of approximately 5.0 and 8.6. The protonation event at 5.0 represented the deprotonation of the pyridinium nitrogen in the **3.1-p** species to generate the **3.1-n** species while the protonation event at 8.6 corresponded to the deprotonation of the alcohol in the **3.1-n** species. While the **3.1-zp** species was a possible protonation state, the titration data for proton A in **3.1** had not indicated that **3.1-zp** is formed at a meaningful concentration as the chemical shift for proton A in **Figure 3.11** (left) was expected to experience a downfield shift which would have increased the chemical shift.

While the pK_a of the pyridine nitrogen and alcohol were easily obtained by tracking the change in peak shift of a proton situated on the aromatic ring, the pK_a of the amine nitrogen in

the derivatized frameworks was difficult to interpret from the change in the shift of the aromatic protons **Figure 3.12** (left). Rather, the amine nitrogen pK_a was obtained by plotting the chemical shift of the benzylic protons vs pH, as illustrated in **Figure 3.12** (right).

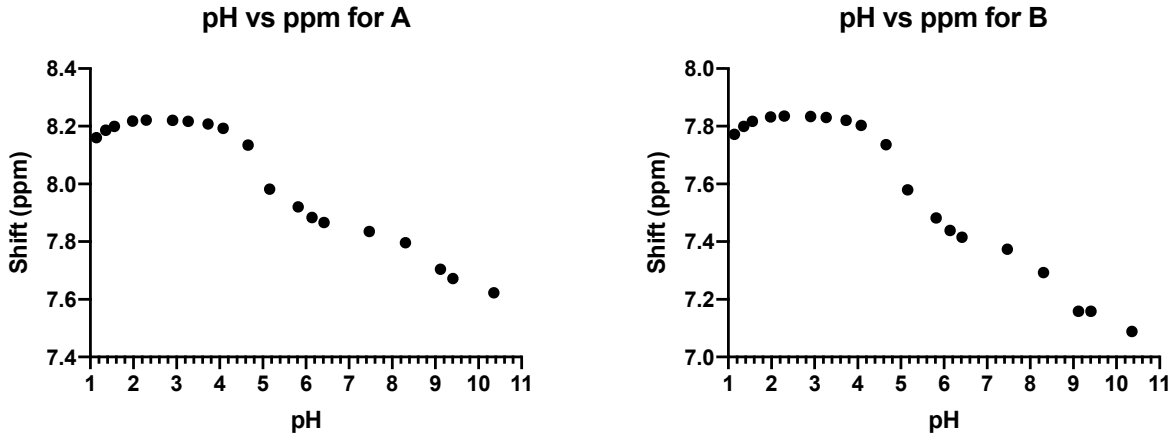

Figure 3.11 Titration data following the chemical shifts of protons A (left) and B (right) (H on C6 and C5 respectively, see **Figure 3.10**) in pyridin-3-ol, **3.1**.

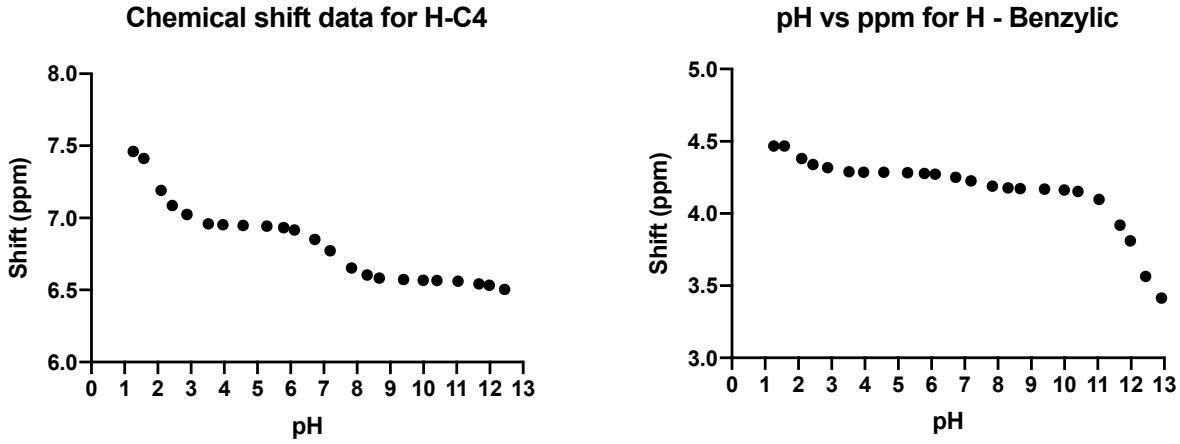

Figure 3.12 pH vs chemical shift data for the H-C4 (left) and benzylic hydrogens (right) in compound **3.2B**.

The titration data for the **3.1** family is shown in **Table 3.1**. Interestingly, the pK_a values for each titratable proton in **3.1D,** which was one of our initial lead compounds, were similar to other pK_a values in the family. The higher resurrection efficacy of compound **3.1D** over dialkylamines or even pyrrolidine as the amine suggests that a change in protonation state was not the critical factor. Instead, the improved efficacy of **3.1D** can likely be attributed to the more effective binding in the active site of OP-aged AChE.

Pyridin-3-ol Derivative (Amine)	pK_a of Pyridine Nitrogen	pK_a of Alcohol	pK_a of Amine Nitrogen
3.1	5.0 ± 0.2	8.6 ± 0.2	-
3.1A (Me_2N)	< 5.4[a]	7.4 ± 0.2	11.0 ± 0.2
3.1C (pyrrolidine)	2.1 ± 0.2	7.5 ± 0.2	11.6 ± 0.2
3.1D ((*R*)-2-Me-pyrrolidine)	2.2 ± 0.2	7.2 ± 0.2	11.7 ± 0.2
3.1E (piperidine)	< 5.9[a]	7.2 ± 0.2	11.0 ± 0.2

[a]The pH range was not sufficient to generate a sigmoidal curve for the specific protonation event.

Table 3.1 Observed pK_a results for the **3.1** family with an assortment of amine leaving groups.

5-OMe-Pyridin-3-ol Derivative (Amine)	pK_a of Pyridine Nitrogen	pK_a of Alcohol	pK_a of Amine Nitrogen
3.2	5.8 ± 0.2	9.3 ± 0.2	-
3.2A (Me_2N)	2.3 ± 0.2	7.4 ± 0.2	11.3 ± 0.2
3.2B (Et_2N)	2.0 ± 0.2	7.2 ± 0.2	12.1 ± 0.2

Table 3.2 Extracted pK_a data for the **3.2** family with select amine leaving groups

6-Me-Pyridin-3-ol Derivative (Amine)	pK_a of Pyridine Nitrogen	pK_a of Alcohol	pK_a of Amine Nitrogen
3.3B (Et_2N)	2.8 ± 0.2	7.4[a] ± 0.2	10.9[a] ± 0.2
3.3C (pyrrolidine)	2.6 ± 0.2	6.9 ± 0.2	11.4 ± 0.2
3.3F (MePrN)	2.9 ± 0.2	7.7[a] ± 0.2	> 6.8

[a]Represents an approximate pK_a value due to the collected data across the pH range.

Table 3.3 Extracted pK_a data for the **3.3** family with an assortment of amine leaving groups.

5-F-Pyridin-3-ol Derivative (Amine)	pK_a of Pyridine Nitrogen	pK_a of Alcohol	pK_a of Amine Nitrogen
3.4	3.2 ± 0.2	7.8 ± 0.2	-
3.4C (pyrrolidine)	0.5 ± 0.2	6.4 ± 0.2	11.2 ± 0.2
3.5C (pyrrolidine)	0.7[a] ± 0.2	6.1 ± 0.2	10.0 ± 0.2

[a]Represents an approximate pK_a value due to the collected data across the pH range.

Table 3.4 Extracted pK_a data for the **3.4** and **3.5** families with the pyrrolidine leaving group.

While plotting the chemical shift of each proton over a wide pH range proved to be valuable, the ^{1}H NMR spectra had additional pieces of remarkable information. Herein, we report that the change in protonation state of a model QMP may be indicated by the coupling constants found between the protons of the pyridine ring. The *J* values for all subsequent discussions will listed be denoted as $J_{x\text{-}y}$ where x and y represent the carbon atoms to which the coupled hydrogens are bonded. Additionally, these coupling constants, unless denoted otherwise, will only represent meta (4-bond) $^4J_{H\text{-}H}$ couplings that are present on the pyridine framework.

Like the graph shown in **Figure 3.11**, the meta coupling constants between the aromatic protons in **3.2** were plotted versus the pH of an aqueous solution. **Table 3.2** indicates that the

two titratable protons for **3.2** have pK_a values of 5.8 and 9.3, corresponding to protonation/deprotonation of the pyridine nitrogen and the alcohol, respectively. Interestingly, these protonation events can be tracked not only by the chemical shifts of the hydrogen atoms, but also by the meta coupling constants in the molecule (**Figure 3.13**). Rather than assigning a protonation state based solely on chemical intuition and typical pK_a values, we sought to find a computational method which could corroborate the variation in coupling constants. Fortunately, robust density functional theory (DFT) methods allow for the coupling constants of a species to be accurately calculated.[7]

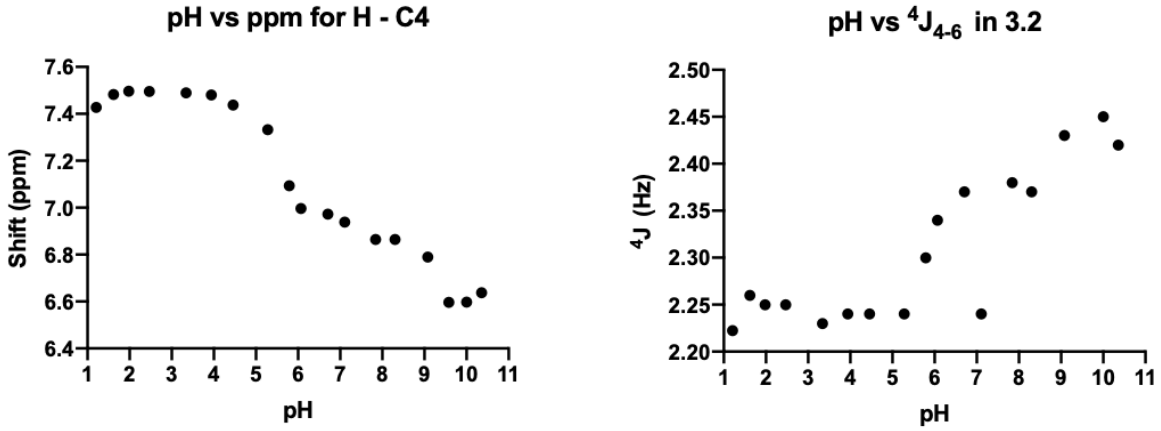

Figure 3.13 Titration data following the peak shift (left) for the H at C4 and meta $^4J_{4-6}$ coupling constant (right) in 5-methoxypyridin-3-ol, **3.2**

Coupling constant data were generated by first obtaining conformations of **3.2**, for each protonation state, using a Monte Carlo search algorithm with the OPLS3e[8] molecular mechanics force field. All subsequent optimizations and calculations were performed with Gaussian 16.[9]

Optimizations followed by vibrational frequency analyses were then performed on each conformation of **3.2** using the B3LYP[10-12]/aug-cc-pVTZ[13] level of theory along with the SMD solvation model for water as the solvent.[14] Optimized stationary points were confirmed to be local minima (all real vibrational frequencies) from the vibrational frequency analyses. The lowest energy conformer was subsequently subjected to a single-point NMR coupling constant calculation using Deng's two step coupling calculation. The first step calculates the Fermi Contact term by uncontracting and augmenting the basis set specified by the user with additional 1s functions for the hydrogen atom.[15] The second step then calculates the spin-dipolar, paramagnetic spin-orbit, and the diamagnetic spin-orbit terms using the initial basis set specified by the user.[15] The four terms are then summed to give the total *J* coupling between the two nuclei.

Our initial investigation of the meta $^4J_{4\text{-}6}$ coupling constants were focused on the **3.2** core framework. Notably, the comparison of the **3.2-p** (pyridinium) and **3.2-d** (phenoxide) protonation states were the simplest to validate experimentally as these states were expected to dominate the population in solution at low and high pH values, respectively. Additionally, the **3.2-n** and **3.2-zp** protonation states were also examined. The calculated $^4J_{4\text{-}6}$ coupling for **3.2-p**, **3.2-n** and **3.2-d**, which were expected to be the most dominant protonation states present at a low, moderate, and high pH were in excellent agreement with the experimental $^4J_{4\text{-}6}$ couplings (**Table 3.5**). The **3.2-zp** protonation state, which was not expected to be the dominant species in solution at any pH, did not indicate agreement between the calculated and experimental $^4J_{4\text{-}6}$ coupling constant.

Experimental pH	Exp. $^4J_{4\text{-}6}$ (Hz)	Calc. $^4J_{4\text{-}6}$ (Hz)
3.3	2.23 ± 0.05	2.25 for **3.2-p**
7.8	2.38 ± 0.05	2.09 for **3.2-zp**
8.3	2.37 ± 0.05	2.33 for **3.2-n**
10.0	2.45 ± 0.05	2.41 for **3.2-d**

Table 3.5 Comparison of the experimental and calculated $^4J_{4\text{-}6}$ coupling constants in **3.2** at a variety of pH values, along with the computed DFT values for specific protonation states.

The remarkable agreement between the experimental and calculated coupling constants shown in **Table 3.5** prompted the investigation of the meta couplings found in compound **3.1**. Notably, **3.1** will only investigate the couplings found in the **3.1-d** and **3.1-p** species as the experimental data over the pH range of approximately 5 – 8 resulted in the overlap of the signals for the H at C-4 and the H at C-5. While the overlap allowed for the extraction of peak shifts as shown in **Figure 3.11**, any coupling information was not distinguishable. However, a comparison of the calculated and experimental $^4J_{2\text{-}4}$ couplings at both low and high pH in **3.1** could be determined and are shown in **Table 3.6**.

Experimental pH	Exp. $^4J_{2\text{-}4}$ (Hz)	Calc. $^4J_{2\text{-}4}$ (Hz)
1.6	2.61 ± 0.05	2.65 for **3.2B-p**
9.4	2.93 ± 0.05	2.85 for **3.2B-d**

Table 3.6 Comparison of the experimental and calculated $^4J_{2\text{-}4}$ coupling constants in **3.1** at a variety of pH values, along with the computed DFT values for specific protonation states.

Like **3.2**, the limited calculated meta coupling constants for **3.1** were similar to the experimental coupling constants. Consequently, we wondered if the meta coupling constants of a QMP could be used to corroborate protonation state assignments generated from the NMR titration data, as illustrated in **Table 3.1** through **Table 3.4**. The QMP **3.2B** was arbitrarily chosen as the model reference. Additionally, while it is known that two theoretical protons A and B couple to each other exactly such that $J_{A\text{-}B} = J_{B\text{-}A}$, the coupling constants for **3.2B** were only measured from the proton corresponding to the H on C-4. Interestingly, at both high and low pH, the experimental data indicated that $J_{4\text{-}6} \neq J_{6\text{-}4}$ (**Figure 3.14**). While the difference between the low pH couplings was approximately 0.1 Hz (**Figure 3.14**), most experimental spectra in this thesis only exhibited differences in the coupling constants of approximately 0.04 Hz. The discrepancy between the coupling constants can likely be attributed to heteronuclear coupling between the H on C-6 and the pyridine nitrogen which, in some cases, is known to broaden the signal of the C-6 protons which are adjacent to the pyridine nitrogen via quadrupolar relaxation.[16] This interaction with the pyridine N was not present with the H on C-4.

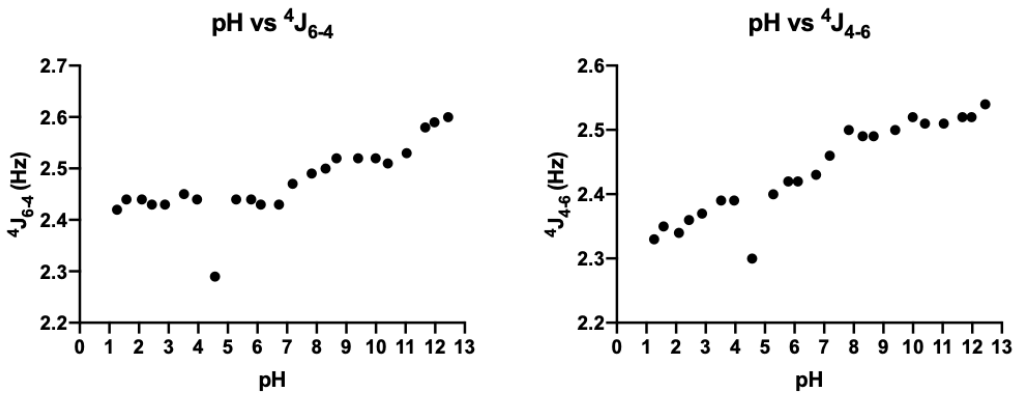

Figure 3.14 pH vs ^4J coupling constants obtained from the peaks corresponding to the NMR signal of the H on C-6 (left) and H on C-4 (right) in **3.2B**, 5-OMe-pyridin-3-ol derivative with the diethylamine (Et_2N) leaving group.

As in **Figure 3.13**, the data shown in **Figure 3.15** (right) indicated that a protonation event at an approximate pH of 2 elicited a small change in the $^4J_{4-6}$ coupling. This change in coupling constant likely correlated to the deprotonation of the pyridine nitrogen in the doubly charged **3.2B-b** species which generated the **3.2B-a** species. Additionally, the protonation event at a pH of 7.2 was also indicated by a small increase in the $^4J_{4-6}$ values. The deprotonation of the amine nitrogen, indicated by a change in ppm (**Figure 3.12**), was not clearly indicated with a marked change in the $^4J_{4-6}$ (**Figure 3.15** right). However, this lack of significant change in the $^4J_{4-6}$

coupling between the **3.2B-za** and **3.2B-d** species correlated well to the calculated data shown in **Table 3.7**.

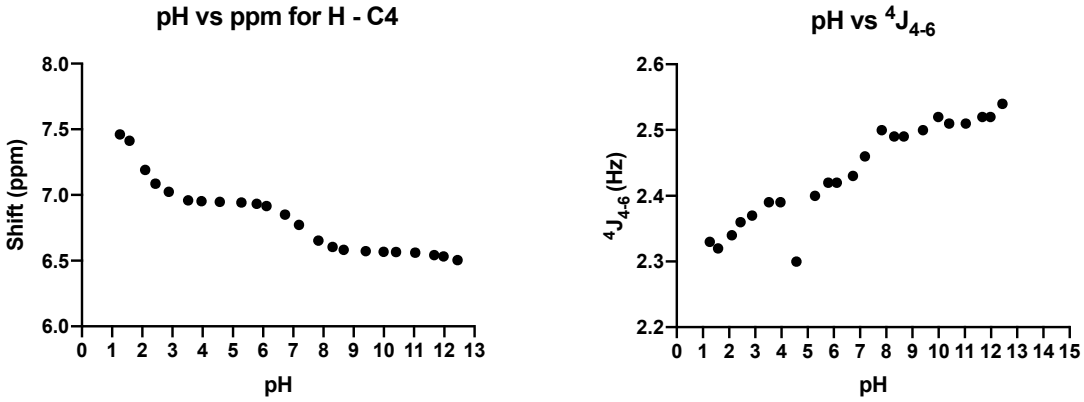

Figure 3.15 Titration data following the peak shift (left) and meta coupling constant (right) in **3.2B**, 5-OMe-pyridin-3-ol derivative with the diethylamine (Et_2N) leaving group.

Experimental pH	Exp. $^4J_{4-6}$ (Hz)	Calc. $^4J_{4-6}$ (Hz)
1.3	2.32 ± 0.05	2.30 for **3.2B-b**
5.3	2.40 ± 0.05	2.26 for **3.2B-a**
8.3	2.49 ± 0.05	2.47 for **3.2B-za**
12.0	2.52 ± 0.05	2.52 for **3.2B-d**

Table 3.7 Comparison of the experimental and calculated $^4J_{4-6}$ coupling constants in **3.2B** at a variety of pH values, along with the computed DFT values for specific protonation states.

While solution-phase NMR can generate a plethora of useful data, NMR is intrinsically a slow method where the data represent an average of all species in solution. Consequently, we sought to find a faster analytical method which could be used to corroborate our initial

protonation assignments. We initially focused on IR spectroscopy as computational simulations of IR spectra were simple to calculate and easily compared to the extant experimental data.

Initial investigations into using IR spectroscopy and computational methods to correlate protonation states, like the NMR study above, focused on using **3.2B**, the 5-OMe-pyridin-3-ol derivative with the diethylamine (Et_2N) leaving group. In the NMR studies, each compound was typically in the 1 mM concentration range, and the solvent was either a 40 mM concentration phosphate buffer or water where both solvents were diluted with 10% D_2O. However, for the IR spectra, **3.2B** was dissolved at a concentration of 220 mM in deionized water. The sample was then titrated with HCl or NaOH to the pH of interest.

Before the experimental IR spectrum was recorded, the IR instrument was blanked with a sample of deionized water which was titrated with HCl or NaOH to be within 0.5 pH units of the sample of interest. Additionally, the deionized water blank made the IR spectra range of 2000 – 3000 cm^{-1} undiscernible. Consequently, all IR spectra will be analyzed in the range of 750 – 1650 cm^{-1}. Experimental IR data for **3.2B** were obtained at pH 7.25 and the spectrum is shown in **Figure 3.16**.

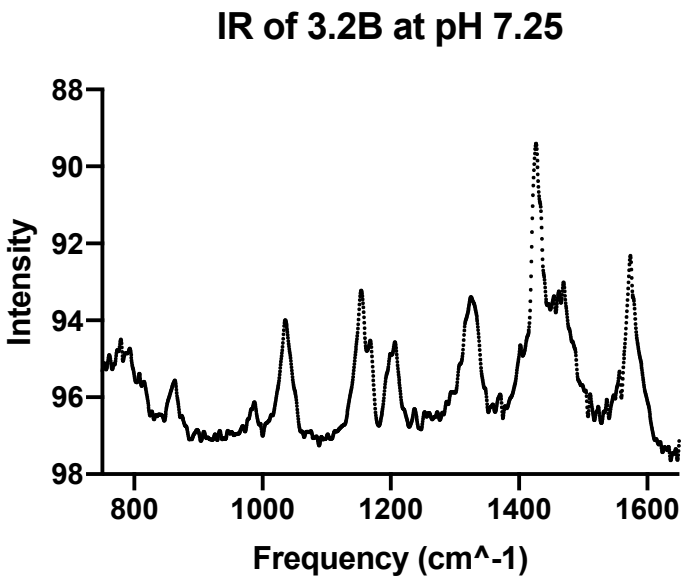

Figure 3.16 IR spectrum of **3.2B** in deionized water at pH 7.25

Additional IR spectra with the overlaid calculated IR, shown as vertical lines, for each protonation state of **3.2B** are shown in

Figure 3.17. Both experimental and calculated spectra were scaled in relation to the IR peak with the largest intensity. All calculated conformations of **3.2B**, for each protonation state, were generated with a Monte Carlo search algorithm using the OPLS3e molecular mechanics force field.[8] The resulting conformations were optimized with the B3LYP[10-12] density functional and the 6-311+G**[17-18] basis set using the SMD[14] solvation model with water as the solvent. Vibrational frequency analyses were performed for each conformation to ensure that only real frequencies were present. The generated vibrational frequencies were not scaled.

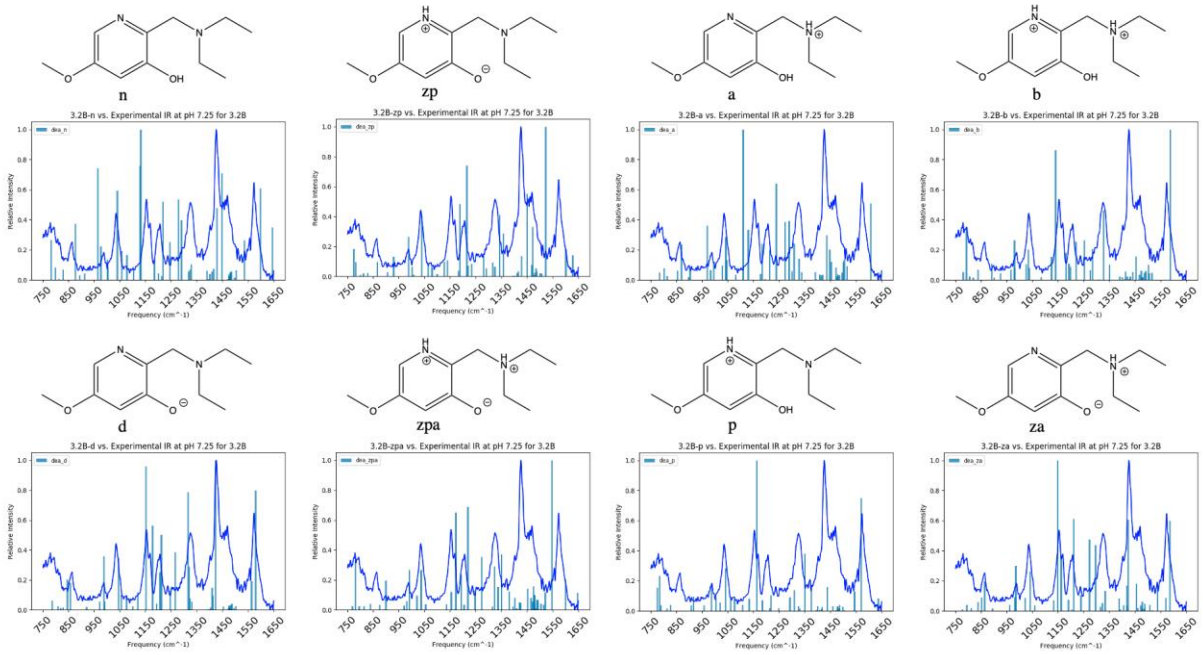

Figure 3.17 Experimental IR spectrum of **3.2B** at pH 7.25 overlaid with the calculated IR spectra for each protonation state (vertical lines). The protonation state is indicated above each image.

An analysis of **Figure 3.16** indicated a variety of IR peaks, with the most notable signatures being at 865, 972, 1050, 1150, 1170, 1200, 1310, 1430, and 1575 cm^{-1} with the peak at 1430 cm^{-1} being the most intense. Of the computed spectra presented in **Figure 3.17**, figures which represent the **3.2B-n, 3.2B-za**, **3.2B-d** and the **3.2B-zp** protonation states bore moderate agreeance with the experimental IR spectra.

Notably, of these four protonation states, three protonation states, **3.2B-za**, **3.2B-d** and **3.2B-zp**, possessed a formal negative charge on the oxygen atom. Each of these species are predicted to have intense bands at approximately 1430 cm^{-1} which agree well with the

experimental band at 1430 cm^{-1} (**Figure 3.16**). Examination of the **3.2B-za**, **3.2B-d** and **3.2B-zp** IR bands at approximately 1430 cm^{-1} with Gaussview 6[19] confirm that the IR band is a C–O stretch.

The calculated spectra for **3.2B-n, 3.2B-za** and **3.2B-d** also showed moderate agreement with the experimental band at 865 cm^{-1} which correlated to a distinct out-of-plane C–H bend from the pyridine framework. Analysis of the computational normal coordinate for that band (with Gaussview) confirmed the motions to be a C–H out-of-plane bending vibration.

Subsequently, we wondered if the C–H out-of-plane bending vibration could be used as a diagnostic for the protonation state of the pyridine nitrogen, while the C–O stretch at 1430 cm^{-1} would be used as a diagnostic for the protonation state of the oxygen atom. Importantly, only the protonation states with a deprotonated pyridine nitrogen in **3.2B** have a C–H out-of-plane bending vibration at approximately 865 cm^{-1}. Similarly, only the calculated protonation states of **3.2B** where the alcohol was anionic possessed the intense C–O stretch at 1430 cm^{-1}.

As the NMR titration data shown in **Table 3.2** indicated that the amine in **3.2B** had a pK_a of approximately 12.2, the amine nitrogen should be protonated at a pH near 7. Subsequently near physiological pH, **3.2B** was determined to primarily be in the **3.2B-za** protonation state. Consequently, we wondered if a plot which contained a Boltzmann weighting of all 121 conformations of **3.2B-za** would provide an accurate representation of the experimental IR spectrum (**Figure 3.18**).

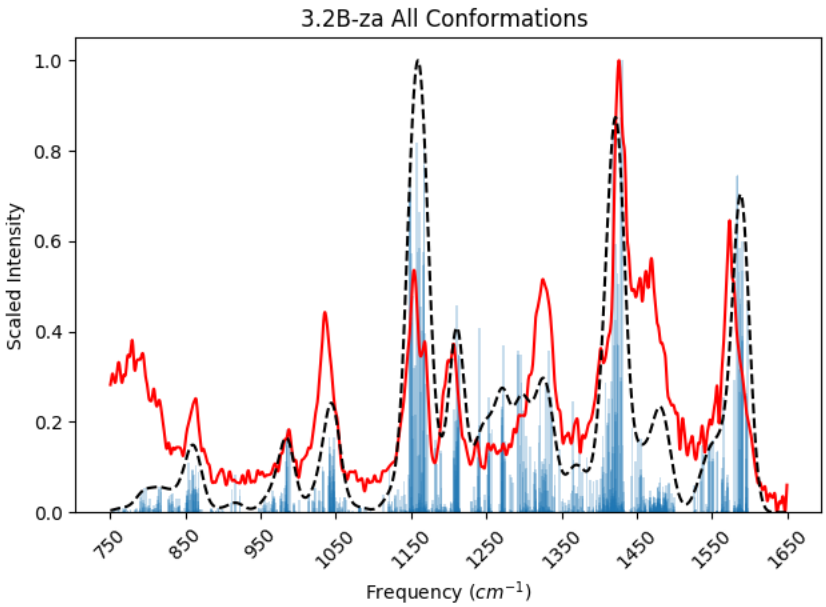

Figure 3.18 Boltzmann distribution of all computed 121 conformations of **3.2B-za** at the B3LYP/6-311+G(d,p) level of theory. The experimental IR of **3.2B** was obtained at a pH of 7.25 in water. The experimental spectrum is shown in red, while a gaussian-broadened spectrum (using a peak broadening of approximately 4 cm^{-1}) of all calculated IR peaks is shown as a dashed line.

Unfortunately, while **Figure 3.18** indicated that the calculated peaks at approximately 870, 980, 1150, and 1570 cm^{-1} were in moderate agreeance with the experimental spectra, the features at approximately 1340 and 1430 cm^{-1} were not representative of the experimental IR. However, it should be noted that the features in the Boltzmann of distribution of **3.2B-za** were heavily weighted towards conformations which contain an NH---O hydrogen bond between the amine nitrogen and the phenoxide. Consequently, we hypothesized that conformations bearing an NH---N hydrogen bond between the amine and pyridine nitrogen might generate a different Boltzmann distribution, which may be more representative of the experimental IR. Two

Boltzmann distributions of **3.2B-za**, representing orientations featuring an NH--O hydrogen bond or an NH--N hydrogen bond are shown in **Figure 3.19**.

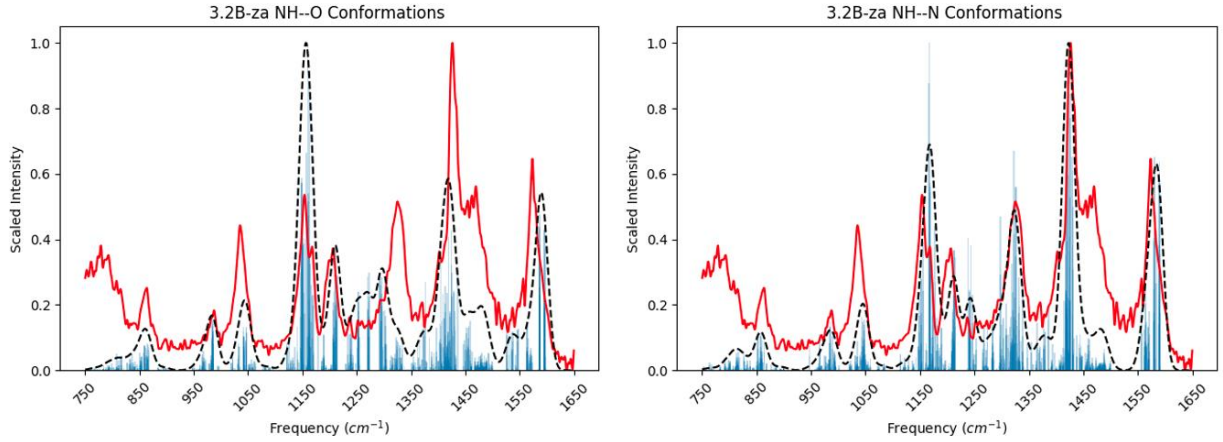

Figure 3.19 Boltzmann distributions of **3.2B-za** calculated at the B3LYP/6-311+G(d,p) level of theory, representing conformations which feature an NH---O shared hydrogen bond (left) and an NH---N hydrogen bond (right). The experimental spectrum is shown in red, while a gaussian-broadened spectrum (using a peak broadening of approximately 4 cm^{-1}) of the calculated IR peaks is shown as a dashed line.

Interestingly, the conformation bearing the NH---N hydrogen bond (**Figure 3.19** right) seemed to more accurately predict the peaks found at approximately 1300 and 1430 cm^{-1}. Additionally, while displaying conformations containing either the NH---O or NH---N shared hydrogen bond is informative, the hydrogen bond is dynamic and is likely situated somewhere between the two atoms. Thus, the dynamic nature of the hydrogen bond might make **3.2B-zp** as well as **3.2B-n** valid protonation states. Boltzmann distributions of all of the calculated IR **3.2B-zp** and **3.2B-n** protonation states are shown in **Figure 3.20**.

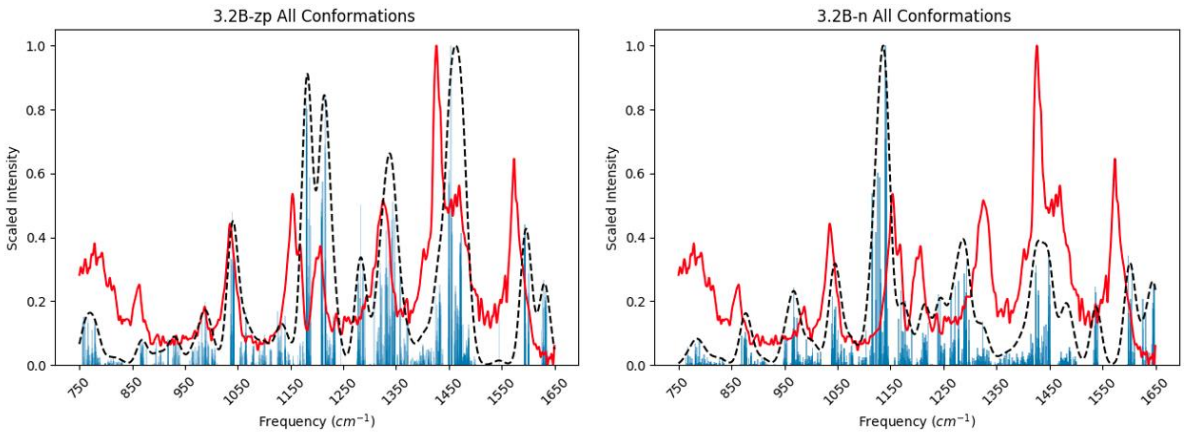

Figure 3.20 Boltzmann distributions featuring the **3.2B-zp** protonation state (left) and the **3.2B-n** protonation state (right) calculated at the B3LYP/6-311+G(d,p) level of theory. The experimental spectrum is shown in red while a gaussian-broadened spectrum (using a peak broadening of approximately 4 cm^{-1}) of all calculated IR peaks is shown as a dashed line.

While both images shown in **Figure 3.20** bear some resemblance to the experimental spectra, the overall agreement between the calculated spectra of **3.2B-zp** and **3.2B-n** relative to the experimental spectrum was poor. Notably, as the **3.2B-n**, **3.2B-za**, and **3.2B-zp** protonation states are isomers with similar electronic energies, these different protonation states could be mixed to generate novel Boltzmann distributions. Consequently, we hypothesized that a Boltzmann distribution of conformations of **3.2B-za** bearing the NH---N hydrogen bond and all conformations of the **3.2B-zp** protonation state might more accurately represent the experimental IR. We also examined a Boltzmann distribution containing conformations of **3.2B-**

za bearing the NH---O hydrogen bond as well as the **3.2B-n** protonation (**Figure 3.21**).

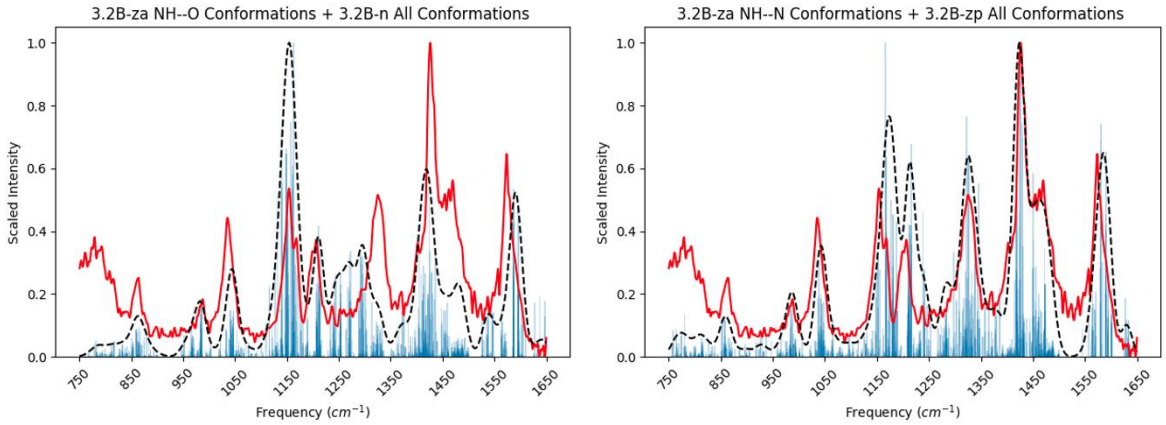

Figure 3.21 Boltzmann distributions featuring **3.2B-za** orientations bearing an NH---O hydrogen bond and the **3.2B-n** conformations (left) and **3.2B-za** conformations bearing the NH---N hydrogen bond and the **3.2B-zp** conformations (right) calculated at the B3LYP/6-311+G(d,p) level of theory. The experimental spectrum is shown in red, while a gaussian-broadened spectrum (using a peak broadening of approximately 4 cm^{-1}) of all calculated IR spectra is shown as a dashed line.

Analysis of **Figure 3.21** indicated that the Boltzmann distribution containing conformations of **3.2B-za** with an NH---N hydrogen bond as well as all conformations of the **3.2B-zp** protonation state bore significant agreeance with the experimental spectrum. However, two regions of the IR shown in **Figure 3.21** (right) at approximately 1250 and 1500 cm^{-1} have calculated bands which are not represented well in the experimental spectra. Interestingly, Gaussview analysis of the vibrational bands at 1500 cm^{-1}, which were only found in the **3.2B-zp** conformations, revealed that the bands are an in-plane NH bend. If the hydrogen

atom is involved in a shared intramolecular NH---N hydrogen bond, perhaps this vibrational mode might be significantly dampened in the experimental spectra. Analysis of the bands at approximately 1250 cm^{-1} in **Figure 3.21** (right) indicated that these bands represent an in-plane symmetric bend of both aromatic hydrogens, and that this vibrational mode is also coupled with an N–H in-plane hydrogen bend. Perhaps the reduced intensity of the 1250 cm^{-1} band in the experimental spectra, could also be explained by an NH--N intramolecular hydrogen bond.

In conclusion, the ^{1}H-^{1}H coupling constant data obtained from NMR as well as the IR data for **3.2B** indicate that near physiological pH, **3.2B** exists primarily as **3.2B-za.** Additionally, while **3.2B-za** might be the prevalent protonation state, the hydrogen atom on the amine nitrogen is involved in a shared hydrogen bond, with the phenoxide oxygen (NH---O) and the pyridine nitrogen (NH---N). This hydrogen bond results in the **3.2B-zp** protonation state conformations being necessary to accurately predict the IR spectra of **3.2B**. Additionally, the titration data which analyzed the chemical shift of various protons on **3.2B** indicated that **3.2B** is near the equivalence point for the deprotonation event of **3.2B-a**. Near the equivalence point, **3.2B** is expected to be present as both the **3.2B-a** and **3.2B-za** protonation states. Consequently, after consideration of both the IR and NMR data presented, future molecular dynamic studies should focus on the **3.2B-a, 3.2B-za** and **3.2B-zp** protonation states as these protonation states have been shown to be the most dominant protonation states for **3.2B** near physiological pH.

References for Chapter 3

1. Quinn, D. M. Acetylcholinesterase: enzyme structure, reaction dynamics, and virtual transition states, *Chem. Rev.* **1987**, 87, 955-979.
2. Bajgar, J.; Jun, D.; Kuča, K.; Fusek, J.; Karasová, J. Z.; Kassa, J.; Cabal, J.; Bláha, V. Inhibition of blood cholinesterases by nerve agents in vitro, *J. Appl. Biomed.* **2009**, 7, 201 – 206.
3. Zhuang, Q.; Franjesevic, A. J.; Corrigan, T. S.; Coldren, W. H.; Dicken, R.; Sillart, S.; Deyong, A.; Yoshino, N.; Smith, J.; Fabry, S.; Fitzpatrick, K.; Blanton, T.G.; Joseph, J.; Yoder, R. J.; McElroy, C. A.; Ekici, Ö. D.; Callam, C. S.; Hadad, C. M. Demonstration of In Vitro Resurrection of Aged Acetylcholinesterase after Exposure to Organophosphorus Chemical Nerve Agents, *J. Med. Chem.,* **2018**, *61*(16), 7034–7042.
4. Greenwood, J. R.; Calkins, D.; Sullivan, A. P.; Shelley, J. C. Towards the comprehensive, rapid, and accurate prediction of the favorable tautomeric states of drug-like molecules in aqueous solution, *J. Comput. Aided Mol. Des.*, **2010**, 24, 591-604.
5. Shelley, J.C.; Cholleti, A.; Frye, L; Greenwood, J.R.; Timlin, M.R.; Uchimaya, M. Epik: a software program for pKa prediction and protonation state generation for drug-like molecules, *J. Comp. Aided Mol. Des.*, **2007**, 21, 681-691.

6. Benzecon, J.; Wittwer, M. B.; Cutting, B.; Smieško, M.; Wagner, B.; Ernst, B., pK_a determination by ^1H NMR spectroscopy – An old methodology revisited, *J. Pharm. Biomed. Anal.*, **2014**, 93, 147-155.

7. Bally, T.; Rablen, P. R., Quantum-Chemical Simulation of H-1 NMR Spectra. 2. Comparison of DFT-Based Procedures for Computing Proton-Proton Coupling Constants in Organic Molecules, *J. Org. Chem.,* **2011**, 76, 4818-4830.

8. Harder, E.; Damm, W.; Maple, J.; Wu, C.; Reboul, M.; Xiang, J. Y.; Wang, L.; Lupyan, D.; Dahlgren, M. K.; Knight, J. L.; Kaus, J. W.; Cerutti, D. S.; Krilov, G.; Jorgensen, W. L.; Abel, R.; Friesner, R. A., OPLS3: A Force Field Providing Broad Coverage of Drug-like Small Molecules and Proteins, *J. Chem. Theory Compu.,* **2016**, 12, 281–296.

9. Frisch, M. J.; Trucks, G. W.; Schlegel, H. B.; Scuseria, G. E.; Robb, M. A.; Cheeseman, J. R.; Scalmani, G.; Barone, V.; Petersson, G. A.; Nakatsuji, H.; Li, X.; Caricato, M.; Marenich, A. V.; Bloino, J.; Janesko, B. G.; Gomperts, R.; Mennucci, B.; Hratchian, H. P.; Ortiz, J. V.; Izmaylov, A. F.; Sonnenberg, J. L.; Williams-Young, D.; Ding, F.; Lipparini, F.; Egidi, F.; Goings, J.; Peng, B.; Petrone, A.; Henderson, T.; Ranasinghe, D.; Zakrzewski, V. G.; Gao, J.; Rega, N.; Zheng, G.; Liang, W.; Hada, M.; Ehara, M.; Toyota, K.; Fukuda, R.; Hasegawa, J.; Ishida, M.; Nakajima, T.; Honda, Y.; Kitao, O.; Nakai, H.; Vreven, T.; Throssell, K.; Montgomery, J. A., Jr.; Peralta, J. E.; Ogliaro, F.; Bearpark, M. J.; Heyd, J. J.; Brothers, E. N.; Kudin, K. N.; Staroverov, V. N.; Keith, T. A.; Kobayashi, R.; Normand, J.; Raghavachari, K.; Rendell, A. P.; Burant, J. C.; Iyengar, S. S.; Tomasi, J.; Cossi, M.; Millam, J. M.; Klene, M.; Adamo, C.; Cammi, R.; Ochterski,

J. W.; Martin, R. L.; Morokuma, K.; Farkas, O.; Foresman, J. B.; Fox, D. J. Gaussian 16, Rev. A. 03 Gaussian, Inc., Wallingford CT, 2016.

10. Becke, A. D., Density-functional Thermochemistry. III. The Role of Exact Change, *J. Chem. Phys.,* **1993**, 98, 5648–5652.

11. Kim, K.; Jordan, K. D. Comparison of Density Functional and MP2 Calculations on the Water Monomer and Dimer, *J. Phys. Chem*., **1994**, 98, 10089–10094.

12. Stephens, P. J.; Devlin, F. J.; Chabalowski, C. F.; Frisch, M. J. Ab Initio Calculation of Vibrational Absorption and Circular Dichroism Spectra Using Density Functional Force Fields, *J. Phys. Chem.,* **1994**, 98, 11623–11627.

13. Kendall, R. A.; Dunning, Thom. H.; Harrison, R. J., Electron affinities of the firstrow atoms revisted. Systematic basis sets and wave functions, *J. Chem. Phys.,* **1992**, 96, 6796-6806.

14. Marenich, A. V.; Cramer, C. J.; Truhlar, D. G. Universal solvation model based on solute electron density and a continuum model of the solvent defined by the bulk dielectric constant atomic surface tensions, *J. Phys. Chem. B.*, **2009**, 113, 6378-6396.

15. Deng, W.; Cheeseman, J. R.; Frisch, M. J., Calculation of Nuclear Spin-Spin Coupling Constants of Molecules with First and Second Row Atoms in Study of Basis Set Dependence, *J. Chem. Theory and Comput.,* **2006,** 2, 1028-1037.

16. Kintzinger, J. P.; Lehn, J. M. Nuclear relaxation and molecular properties Part I. ^{14}N nuclear quadrupolar relaxation ^{1}H line shapes in nitrogen-containing heterocycles, *J. Mol. Phys.,* **1968**, *14*(2), 133-145

17. McLean, A. D.; Chandler, G. S. Contracted Gaussian-basis sets for molecular calculations. 1. 2nd row atoms, Z-11-18, *J. Chem Phys.,* **1980**, 72, 5639-5648.

18. Rahavachari, K.; Binkley, J. S.; Seeger, R.; Pople, J. A. Self-Consistent Molecular Orbital Methods. 20. Basis set for correlated wave functions, *J. Chem. Phys.,* **1980**, 72, 650-654.

19. Dennington, R.; Todd, A. K.; Millam, J. M., Semichem. Inc., Shawnee Mission, KS, **2016**

Bibliography

References from Chapter 1:

(1) Gunnell, D.; Eddleston, M.; Phillips, M.R.; Konradsen, F. The global distribution of fatal pesticide self-poisoning: Systematic review., *BMC Public Health,* 7, 357 (**2007**).

(2) Tucker, J. B. *War of Nerves*; Anchor, 2007.

(3) Franjesevic, A. J.; Sillart, S. B.; Beck, J. M.; Vyas, S.; Callam, C. S.; Hadad, C. M. Resurrection and Reactivation of Acetylcholinesterase and Butyrylcholinesterase., *Chem. Eur. J.,* **2018**, 1–36.

(4) Pitschmann, V. Overall View of Chemical and Biochemical Weapons, *Toxins*, **2014**, 6 (6): 1761–1784

(5) Central Intelligence Agency. Iraq's Chemical Warfare Program https://www.cia.gov/library/reports/general-reports-1/iraq_wmd_2004/chap5.html (accessed Feb 03, 2020).

(6) Stone, R. Chemical Martyrs, *Science,* **2018**, 359 (6371), 20–25.

(7) The White House. Government Assessment of the Syrian Government's Use of Chemical Weapons on August 21, 2013 https://www.whitehouse.gov/the-pressoffice/2013/08/30/government-assessment-syrian-government-s-use-chemicalweapons-august-21 (accessed Feb 03, 2020).

(8) The White House. United States Government Assessment of the Assad Regime's Chemical Weapons Use on April 13, 2018 https://whitehouse.gove/briefings-

statements/united-states-government-assessment-assad-regimes-chemical-weapons-use (accessed Feb 03, 2020)

(9) Eileen Ng. Malaysia charges two women in death of Kim Jong-nam. *The Globe and Mail*. https://web.archive.org/web/20170306034317/http://www.theglobeandmail.com/news/world/north-korean-diplomats-in-malaysia-seek-kim-jong-nams-body/article34157158/ (Accessed Feb 07, 2020)

(10) Kim Jong-nam death: suspect Siti Aisyah released after charge dropped *The Guardian* https://www.theguardian.com/world/2019/mar/11/kim-jong-nam-trial-siti-aisyah-released-after-charge-dropped (Accessed Feb 07, 2020)

(11) Asthana, A.; Roth, A.; Harding, L.; MacAskill, E. Russian Spy Poisoning: Theresa May Issues Ultimatum to Moscow. *The Guardian*. March 13, 2018. https://www.theguardian.com/uk-news/2018/mar/12/russia-highly-likely-to-be-behind-poisoning-of-spy-says-theresa-may (Accessed Feb 07, 2020)

(12) A, Harriet. Amesbury Incident Latest: Wiltshire Couple Were Exposed to Novichok Nerve Agent, Police Say. *The Independent, Independent Digital News and Media* July 4, 2018. www.independent.co.uk/news/uk/home-news/amesbury-poisoning-latest-novichock-metropolitan-police-neil-basu-professor-dame-sally-davies-a8431916.html (Accessed Feb 12, 2020)

(13) Summary Of The Report On Activities Carried Out In Support Of A Request For Technical Assistance By The United Kingdom Of Great Britain And Northern Ireland (Technical Assistance Visit (Tav) 02/18), OPCW, April 2018.

(14) Beck, J. M.; Hadad, C. M. Reaction Profiles of the Interaction between Sarin and Acetylcholinesterase and the S203C Mutant: Model Nucleophiles and QM/MM Potential Energy Surfaces, *Chem. Biol. Interact.,* **2010**, *187* (1–3), 220–224.

(15) Yanzi, Z.; Shenglong, W.; Yingkai, Z. Catalytic Reaction Mechanism of Acetylcholinesterase Determined by Born-Oppenheimer Ab Initio QM/MM Molecular Dynamics Simulations, *J. Phys. Chem. B.,* **2010**, *114, 26, 8817-8825.*

(16) Topczewski, J. J.; Quinn, D. M Kinetic Assessment of N-methyl-2-methoxypyridinium Species as Phosphate Anion Methylating Agents, *Org. Lett.,* **2013**, *15* (5), 1084–1087.

(17) Worek, F.; Thiermann, H. The Value of Novel Oximes for Treatment of Poisoning by Organophosphorus Compounds, *Pharmacol Ther.,* **2013,** 139, 249-259.

(18) Zhuang, Q.; Franjesevic, A. J.; Corrigan, T. S.; Coldren, W. H.; Dicken, R.; Sillart, S.; Deyong, A.; Yoshino, N.; Smith, J.; Fabry, S.; Fitzpatrick, K.; Blanton, T.G.; Joseph, J.; Yoder, R. J.; McElroy, C. A.; Ekici, Ö. D.; Callam, C. S.; Hadad, C. M. Demonstration of In Vitro Resurrection of Aged Acetylcholinesterase after Exposure to Organophosphorus Chemical Nerve Agents, *J. Med. Chem.,* **2018**, *61* (16), 7034–7042.

(19) Border. S. E.; Pavlovic. R. Z.; Zhiquan. L.; Badjic. D. J. Removal of Nerve Agent Simulants from Water Using Light Responsive Molecular Baskets, *J. Am. Chem. Soc.,* **2017**, *139* (51), 18496-18499

(20) Mercey, G.; Verdelet, T.; Renou, J.; Kliachyna, M.; Baati, R.; Nachon, F.; Jean, L.; Renard, P. Y. Reactivators of Acetylcholinesterase Inhibited by Organophosphorus Nerve Agents, *Acc. Chem. Res.,* **2012**, 45, 5, 756-766

(21) Valentin, C. D.; Freccero, M.; Zanaletti, Riccardo.; Sarzi-Amadè, M. o-Quinone Methide as Alkylating Agent of Nitrogen, Oxygen, and Sulfur Nucleophiles. The Role of H-Bonding and Solvent Effects on the Reactivity through a DFT Computational Study, *J. Am. Chem. Soc.*, **2001**, 123, 34, 8366-8377.

References from Chapter 2:

(1) Kolesnichenko. I. V.; Anslyn. E. V. Practical Applications of Supramolecular Chemistry, *Chem. Soc. Rev.* **2017**, 46, 2385-2390

(2) You, L.; Zha, D.; Anslyn, E. V. Recent Advances in Supramolecular Analytical Chemistry Using Optical Sensing, *Chem. Rev.* **2015**, 115, 15, 7840–7892.

(3) Maleknia, S.; Brodbelt, J. Gas-phase Selectivities of Crown Ethers for Alkali Metal Complexation, *J. Am. Chem. Soc.* **1992**, 114, 4295–4298.

(4) Border, S. E.; Pavlovic, R. Z.; Zhiquan, L.; Badjic, J. D. Removal of Nerve Agent Simulants from Water Using Light Responsive Molecular Baskets *J. Am. Chem. Soc*. **2017**, 139, 18496−18499

(5) Pavlovic, R. Z.; Lei, Z.; Gueney, M.; Lalisse, R. F.; Hopf, R. G.; Gallucci, J.; Moore, C.; Xie, H.; Hadad, C. M.; Badjic, J. D. Multivalent C−H···Cl/Br−C Interactions Directing the Resolution of Dynamic and Twisted Capsules, *Chem. Eur. J.,* **2019**, 25, 13124-13130.

(6) Li, Y.; Vander Griend, D. A.; Flood, A. H. Modelling Triazolophane-halide Binding Equilibria Using Sivvu Analysis of UV-vis Titration Data Recorded Under Medium Binding Conditions, *Supramolec. Chem.* **2009**, 21, 111-117

(7) Frisch, M. J.; Trucks, G. W.; Schlegel, H. B.; Scuseria, G. E.; Robb, M. A.; Cheeseman, J. R.; Scalmani, G.; Barone, V.; Petersson, G. A.; Nakatsuji, H.; Li, X.; Caricato, M.; Marenich, A. V.; Bloino, J.; Janesko, B. G.; Gomperts, R.; Mennucci, B.; Hratchian, H. P.; Ortiz, J. V.; Izmaylov, A. F.; Sonnenberg, J. L.; Williams-Young, D.; Ding, F.; Lipparini, F.; Egidi, F.; Goings, J.; Peng, B.; Petrone, A.; Henderson, T.; Ranasinghe, D.; Zakrzewski, V. G.; Gao, J.; Rega, N.; Zheng, G.; Liang, W.; Hada, M.; Ehara, M.; Toyota, K.; Fukuda, R.; Hasegawa, J.; Ishida, M.; Nakajima, T.; Honda, Y.; Kitao, O.; Nakai, H.; Vreven, T.; Throssell, K.; Montgomery, J. A., Jr.; Peralta, J. E.; Ogliaro, F.; Bearpark, M. J.; Heyd, J. J.; Brothers, E. N.; Kudin, K. N.; Staroverov, V. N.; Keith, T. A.; Kobayashi, R.; Normand, J.; Raghavachari, K.; Rendell, A. P.; Burant, J. C.; Iyengar, S. S.; Tomasi, J.; Cossi, M.; Millam, J. M.; Klene, M.; Adamo, C.; Cammi, R.; Ochterski, J. W.; Martin, R. L.; Morokuma, K.; Farkas, O.; Foresman, J. B.; Fox, D. J. Gaussian 16, Rev. A. 03 Gaussian, Inc., Wallingford CT, 2016.

(8) Chhetri. B. K.; Lavoie. S.; Sweeney-Jones. A. M.; Kubanek. J. Recent Trends in the Structural Revision of Natural Products*, Nat. Prod. Rep.*, **2018**, 35, 1015-1015.

(9) Chhetri. B. K.; Lavoie. S.; Sweeney-Jones. A. M.; Kubanek. J. Recent Trends in the Structural Revision of Natural Products, *Nat. Prod. Rep.*, **2018**, 35, 514-531.

(10) Keith. T. A.; Bader. R. F. W. Calculation of Magnetic Response Properties Using Atoms in Molecules, *Chem. Phys. Lett.* **1992**, 194, 1-8.

(11) Keith, T. A.; Bader, R. F. W. Calculation of Magnetic Response Properties Using a Continuous Set of Gauge Transformations, *Chem. Phys. Lett.* **1993**, 210, 223-31.

(12) McWeeny, R. Perturbation Theory for the Fock-Dirac Density Matrix, *Phys. Rev.* **1962**, 126, 1028–1034.

(13) Wolinski, K.; Hinton, J. F.; Pulay, P. Efficient Implementation of the Gauge-independent Atomic Orbital Method for NMR Chemical Shift Calculations, *J. Am. Chem. Soc.* **1990**, 112, 8251–8260.

(14) Ditchfield, R. Self-consistent Perturbation Theory of Diamagnetism, *Mol. Phys.* **1974**, 27, 789–807.

(15) Cheeseman, J. R. A Comparison of Models for Calculating Nuclear Magnetic Resonance Shielding Tensors, *J. Chem. Phys*. **1996**, 104, 5497–5509.

(16) Becke, A. D. Density-functional Thermochemistry. III. The Role of Exact Change, *J. Chem. Phys.* **1993**, 98, 5648–5652.

(17) Kim, K.; Jordan, K. D. Comparison of Density Functional and MP2 Calculations on the Water Monomer and Dimer, *J. Phys. Chem*. **1994**, 98, 10089–10094.

(18) Stephens, P. J.; Devlin, F. J.; Chabalowski, C. F.; Frisch, M. J. Ab Initio Calculation of Vibrational Absorption and Circular Dichroism Spectra Using Density Functional Force Fields, *J. Phys. Chem.* **1994**, 98, 11623–11627.

(19) Zhao, Y.; Truhlar, D. G. Density Functionals with Broad Applicability in Chemistry, *Acc. Chem. Res.* **2008**, 41, 157–167.

(20) Ditchfield, R.; Hehre, W. J.; Pople, J. A. Self-Consistent Molecular-Orbital Methods. IX. An Extended Gaussian-Type Basis for Molecular-Orbital Studies of Organic Molecules, *J. Chem. Phys.* **1971**, 54, 724–728.

(21) Hehre, W. J.; Ditchfield, K.; Pople, J. A. Self-Consistent Molecular Orbital Methods. XIV. An Extended Gaussian-Type Basis for Molecular Obrital Studies of Organic Molecules. Inclusion of Second Row Elements, *J. Chem. Phys.* **1972**, 56, 2257–2261.

(22) Hariharan, P. C.; Pople, J. A. Accuracy of AHn Equilibrium Geometries by Single Determinant Molecular Orbital Theory, *Mol. Phys.* **1974**, 27, 209–214.

(23) Gordon, M. S. The Isomers of Silacyclopropane, *Chem. Phys. Lett*. **1980**, 76, 163–168.

(24) Hariharan, P. C.; Pople, J. A. The Influence of Polarization Functions on Molecular Orbital Hydrogenation Energy, *Theor. Chim. Acta.* **1973**, 28, 213–222.

(25) McLean, A. D.; Chandler, G. S. Contracted Gaussian Basis Sets for Molecular Calculations. I. Second Row Atoms, Z=11-18, *J. Chem. Phys.* **1980**, 72, 5639–5648.

(26) Krishnan, R.; Binkley, J. S.; Seeger, R.; Pople, J. A. Self-consistent Molecular Orbital Methods. XX. A Basis Set for Correlated Wave Functions, *J. Chem. Phys.* **1980**, 72, 650–654.

(27) Hay, P. J. Gaussian Basis Sets for Molecular Calculations. The Representation of 3d Orbitals in Transition-metal Atoms, *J. Chem. Phys.* **1977**, 66, 4377–4384.

(28) Raghavachari, K.; Trucks, G. W. Highly Correlated Systems. Excitation Energies of First Row Transition Metals Sc-Cu, *J. Chem. Phys.* **1989**, 91, 1062–1065.

(29) Wachters, A. J. H. Gaussian Basis Sets for Molecular Wavefunctions Containing Third-Row Atoms, *J. Chem. Phys.* **1970**, 52, 1033–1036.

References from Chapter 3:

(1) Kolesnichenko. I. V.; Anslyn. E. V. Practical Applications of Supramolecular Chemistry, *Chem. Soc. Rev.* **2017**, 46, 2385-2390

(2) You, L.; Zha, D.; Anslyn, E. V. Recent Advances in Supramolecular Analytical Chemistry Using Optical Sensing, *Chem. Rev.* **2015**, 115, 15, 7840–7892.

(3) Maleknia, S.; Brodbelt, J. Gas-phase Selectivities of Crown Ethers for Alkali Metal Complexation, *J. Am. Chem. Soc.* **1992**, 114, 4295–4298.

(4) Border, S. E.; Pavlovic, R. Z.; Zhiquan, L.; Badjic, J. D. Removal of Nerve Agent Simulants from Water Using Light Responsive Molecular Baskets *J. Am. Chem. Soc*. **2017**, 139, 18496−18499

(5) Pavlovic, R. Z.; Lei, Z.; Gueney, M.; Lalisse, R. F.; Hopf, R. G.; Gallucci, J.; Moore, C.; Xie, H.; Hadad, C. M.; Badjic, J. D. Multivalent C−H···Cl/Br−C Interactions Directing the Resolution of Dynamic and Twisted Capsules, *Chem. Eur. J.,* **2019**, 25, 13124-13130.

(6) Li, Y.; Vander Griend, D. A.; Flood, A. H. Modelling Triazolophane-halide Binding Equilibria Using Sivvu Analysis of UV-vis Titration Data Recorded Under Medium Binding Conditions, *Supramolec. Chem.* **2009**, 21, 111-117

(7) Frisch, M. J.; Trucks, G. W.; Schlegel, H. B.; Scuseria, G. E.; Robb, M. A.; Cheeseman, J. R.; Scalmani, G.; Barone, V.; Petersson, G. A.; Nakatsuji, H.; Li, X.; Caricato, M.; Marenich, A. V.; Bloino, J.; Janesko, B. G.; Gomperts, R.; Mennucci, B.; Hratchian, H. P.; Ortiz, J. V.; Izmaylov, A. F.; Sonnenberg, J. L.; Williams-Young, D.; Ding, F.; Lipparini, F.; Egidi, F.; Goings, J.; Peng, B.; Petrone, A.; Henderson, T.; Ranasinghe, D.; Zakrzewski, V. G.; Gao, J.; Rega, N.; Zheng, G.; Liang, W.; Hada, M.; Ehara, M.; Toyota, K.; Fukuda, R.; Hasegawa, J.; Ishida, M.; Nakajima, T.; Honda, Y.; Kitao, O.; Nakai, H.; Vreven, T.; Throssell, K.; Montgomery, J. A., Jr.; Peralta, J. E.; Ogliaro, F.; Bearpark, M. J.; Heyd, J. J.; Brothers, E. N.; Kudin, K. N.; Staroverov, V. N.; Keith, T. A.; Kobayashi, R.; Normand, J.; Raghavachari, K.; Rendell, A. P.; Burant, J. C.; Iyengar, S. S.; Tomasi, J.; Cossi, M.; Millam, J. M.; Klene, M.; Adamo, C.; Cammi, R.; Ochterski, J. W.; Martin, R. L.; Morokuma, K.; Farkas, O.; Foresman, J. B.; Fox, D. J. Gaussian 16, Rev. A. 03 Gaussian, Inc., Wallingford CT, 2016.

(8) Chhetri. B. K.; Lavoie. S.; Sweeney-Jones. A. M.; Kubanek. J. Recent Trends in the Structural Revision of Natural Products*, Nat. Prod. Rep.*, **2018**, 35, 1015-1015.

(9) Chhetri. B. K.; Lavoie. S.; Sweeney-Jones. A. M.; Kubanek. J. Recent Trends in the Structural Revision of Natural Products, *Nat. Prod. Rep.*, **2018**, 35, 514-531.

(10) Keith. T. A.; Bader. R. F. W. Calculation of Magnetic Response Properties Using Atoms in Molecules, *Chem. Phys. Lett.* **1992**, 194, 1-8.

(11) Keith, T. A.; Bader, R. F. W. Calculation of Magnetic Response Properties Using a Continuous Set of Gauge Transformations, *Chem. Phys. Lett.* **1993**, 210, 223-31.

(12) McWeeny, R. Perturbation Theory for the Fock-Dirac Density Matrix, *Phys. Rev.* **1962**, 126, 1028–1034.

(13) Wolinski, K.; Hinton, J. F.; Pulay, P. Efficient Implementation of the Gauge-independent Atomic Orbital Method for NMR Chemical Shift Calculations, *J. Am. Chem. Soc.* **1990**, 112, 8251–8260.

(14) Ditchfield, R. Self-consistent Perturbation Theory of Diamagnetism, *Mol. Phys.* **1974**, 27, 789–807.

(15) Cheeseman, J. R. A Comparison of Models for Calculating Nuclear Magnetic Resonance Shielding Tensors, *J. Chem. Phys*. **1996**, 104, 5497–5509.

(16) Becke, A. D. Density-functional Thermochemistry. III. The Role of Exact Change, *J. Chem. Phys.* **1993**, 98, 5648–5652.

(17) Kim, K.; Jordan, K. D. Comparison of Density Functional and MP2 Calculations on the Water Monomer and Dimer, *J. Phys. Chem*. **1994**, 98, 10089–10094.

(18) Stephens, P. J.; Devlin, F. J.; Chabalowski, C. F.; Frisch, M. J. Ab Initio Calculation of Vibrational Absorption and Circular Dichroism Spectra Using Density Functional Force Fields, *J. Phys. Chem.* **1994**, 98, 11623–11627.

(19) Zhao, Y.; Truhlar, D. G. Density Functionals with Broad Applicability in Chemistry, *Acc. Chem. Res.* **2008**, 41, 157–167.

(20) Ditchfield, R.; Hehre, W. J.; Pople, J. A. Self-Consistent Molecular-Orbital Methods. IX. An Extended Gaussian-Type Basis for Molecular-Orbital Studies of Organic Molecules, *J. Chem. Phys.* **1971**, 54, 724–728.

(21) Hehre, W. J.; Ditchfield, K.; Pople, J. A. Self-Consistent Molecular Orbital Methods. XIV. An Extended Gaussian-Type Basis for Molecular Obrital Studies of Organic Molecules. Inclusion of Second Row Elements, *J. Chem. Phys.* **1972**, 56, 2257–2261.

(22) Hariharan, P. C.; Pople, J. A. Accuracy of AHn Equilibrium Geometries by Single Determinant Molecular Orbital Theory, *Mol. Phys.* **1974**, 27, 209–214.

(23) Gordon, M. S. The Isomers of Silacyclopropane, *Chem. Phys. Lett*. **1980**, 76, 163–168.

(24) Hariharan, P. C.; Pople, J. A. The Influence of Polarization Functions on Molecular Orbital Hydrogenation Energy, *Theor. Chim. Acta.* **1973**, 28, 213–222.

(25) McLean, A. D.; Chandler, G. S. Contracted Gaussian Basis Sets for Molecular Calculations. I. Second Row Atoms, Z=11-18, *J. Chem. Phys.* **1980**, 72, 5639–5648.

(26) Krishnan, R.; Binkley, J. S.; Seeger, R.; Pople, J. A. Self-consistent Molecular Orbital Methods. XX. A Basis Set for Correlated Wave Functions, *J. Chem. Phys.* **1980**, 72, 650–654.

(27) Hay, P. J. Gaussian Basis Sets for Molecular Calculations. The Representation of 3d Orbitals in Transition-metal Atoms, *J. Chem. Phys.* **1977**, 66, 4377–4384.

(28) Raghavachari, K.; Trucks, G. W. Highly Correlated Systems. Excitation Energies of First Row Transition Metals Sc-Cu, *J. Chem. Phys.* **1989**, 91, 1062–1065.

(29) Wachters, A. J. H. Gaussian Basis Sets for Molecular Wavefunctions Containing Third-Row Atoms, *J. Chem. Phys.* **1970**, 52, 10